arXiv:2111.09602v1 [cond-mat.other] 18 Nov 2021

Minimal set of crystallographic descriptors for sorption properties in hypothetical Metal Organic Frameworks: Role in sequential learning optimization

Giovanni Trezza, Luca Bergamasco, Matteo Fasano, Eliodoro Chiavazzo*
Department of Energy, Politecnico di Torino, C.so Duca degli Abruzzi 24, Torino 10129, Italy

Abstract

Several studies have been recently reported in the literature on sorption properties of MOFs with a number of organic sorbates, such as ethanol and methanol. Surprisingly, still few studies have been reported on water sorbate despite its large availability, low cost and environmental sustainability, and the screening of a large number of hypothetical MOFs-water working pairs for engineering applications is still challenging. Based on a recently reported database of over 5000 hypothetical MOFs, a first contribution of this study is the identification of the minimal set of crystallographic descriptors underpinning the most important sorption properties of MOFs for CO_2 and, importantly, for H_2O. Furthermore, a comprehensive comparison of several Sequential Learning (SL) algorithms for MOFs properties optimization is carried out and the role played by the above minimal set of crystallographic descriptors clarified. In sorption-based energy transformations, thermodynamic limits of important figures of merit (e.g. maximum specific energy) depend both on operating conditions and equilibrium sorption properties in a wide range of sorbate coverage values. The access to the latter properties is often incomplete, with essential quantities such as equilibrium adsorption isotherms spanning over the full sorbate coverage range and values of the isosteric heat being only partially available. As a result, this may prevent the computation of objective functions during the optimization procedure. We propose a fast procedure for optimizing specific energy in a closed sorption energy storage system with the only access to the water Henry coefficient at a fixed temperature value and to the specific surface area.

Keywords *Metal Organic Frameworks, Sequential Learning, Thermal Energy Storage*

Introduction

Metal Organic Frameworks (MOFs) are crystalline compounds consisting of metal ions and organic linkers, characterized by tunable porosity and incredibly high surface area [1]. Due to their unique properties, MOFs have recently attracted remarkable attention in a wide range of different fields, including gas/vapour separation [2], reaction catalysis [3], drug delivery [4], energy storage and heat transformations [5, 6]. Given their nature of porous adsorbent materials, an intensively active research is focused on the use of MOFs for CO_2 capture, towards the development of effective technologies for mitigating green-house gas emissions [7]. Recently, MOFs have been also employed in adsorption-based atmospheric water harvesting driven by solar thermal energy [8, 9]. In general, when dealing with application of engineering relevance, different inlet gas streams, variable operating conditions, and target properties tailored per each specific case make it challenging to identify an ideal MOF crystal for all applications [10], thus leading to a fragmented case-by-case optimization problem.

Hence, MOFs require proper and efficient methods for tailoring their features according to target properties of interest in each specific application. The latter is everything but an easy task. In fact, due to the myriad of degrees of freedom for MOFs structure and composition, more than 100 trillion

*Corresponding author: eliodoro.chiavazzo@polito.it

compounds have been hypothesized [11], while almost 100000 have been synthesized so far [12]. High-throughput computational screening and machine learning have been recently adopted to analyse large MOF datasets. Such computational tools allow to identify significant correlations between nanoscale features and observable macroscale properties [13, 14], and to select the most suitable crystal for a given application case. A few representative examples are provided by gas-gas separation (D_2/H_2 [15], O_2/N_2 [16], CO/N_2 [17], CO_2/H_2 [18], ethane/ethylene [19], and other gas mixtures [20]), enantioselectivity of chemical compounds [21], gas adsorption (CO_2 [22], CH_4 [23], H_2 [24], thiol [25], organosulfurs [26], acetylene [27]) and combinations thereof [28, 29]. Several computational explorations of MOFs datasets have been carried out also for biomedical (drug delivery [30]), mechanical (CO_2 Brayton cycle [31], osmotic heat engine [32]) and energy applications (heat pumps/chillers [33, 34], thermal energy storage [35]).

In this context, modern *Sequential Learning* (SL) algorithms are emerging as particularly efficient tools for exploring the material high dimensional (crystallographic) feature space. In particular, while evaluating an objective black-box function through demanding physical or numerical experiments, SL tools can provide a well-orchestrated procedure to rationally navigate the high-dimensional parameter (feature) space. Thus, given an initial pool of evaluation points, one can sequentially choose the next experiment to carry out [36, 37], without relying on a naive random guessing. Rather general techniques have been proposed in the area of material science holding the promise to accelerate materials discovery and research [38], with a number of Authors reporting successful use of SL approaches in this field. Aggarwal *et al.* [39], by means of optimal experimental design, successfully characterized a substrate under a thin film. Seko *et al.* [40] found the compound with the highest melting temperature in a given ensemble of candidate materials with less attempts than a naive random choice. Kiyohara *et al.* [41] accelerated the search of a stable interface structure with respect to a traditional *brute force* approach. Dehghannasiri *et al.* [42] efficiently guided experiments to design the shape memory alloy with the lowest energy dissipation at a given temperature. Needless to say that the identification of the parameter space is a very important preliminary step when implementing SL algorithms. Here, we choose to specifically focus on MOFs properties as gas/vapour sorbent materials, since those are particularly relevant for energy applications.

The first important objective of this work is the identification of the minimal set of MOFs features (or *descriptors*) ruling critical adsorption properties in the low-coverage regime, i.e. the Henry solubility coefficients for both CO_2-MOFs and, importantly, H_2O-MOFs working pairs. The above minimal set represent the important crystallographic features underpinning a given adsorption property of interest. In this sense, each minimal set of descriptors is here referred to as the *genetic code* for a given property, and it is identified as described below.

First, we curate and enhance MOF data from a recently developed library made of 8206 compounds generated computationally [43]. Each Crystallographic Information File (CIF) representing a given material is first featurized by means of 1557 Classical Force-field Inspired Descriptors (CFID) [44] taking into account both chemical and structural parameters. Subsequently, we train and validate regression models of target properties involved in heat storage applications, such as Henry coefficients and working capacity. These models are obtained by means of AutoMatminer [45], which is able to automatically find the best pipeline, clean the database, reduce the features, choose the model and tune its hyperparameters. The final ranking and selection of the minimal set of descriptors is finally performed by evaluating the importance of each feature on the models outputs by means of the Kernel SHAP interpretation algorithm [46].

Upon identification of the above crystallographic *genetic code* of sorption properties in MOFs, we investigate its role when using SL algorithms. Therefore, we compare the performance of three different SL methodologies aiming at maximizing H_2O and CO_2 Henry coefficients, and CO_2 working capacity: (a) random Forests with Uncertainty Estimates for Learning Sequentially (FUELS [47]); (b) kriging algorithm [48]; (c) COMmon Bayesian Optimization Library (COMBO) [49]. For each SL methodology, we compare several strategies for choosing the next material to test, combining the

exploration of high-uncertainty regions with the *exploitation* of high-performing candidates. Importantly, we analyse the SL performance using both the minimal subset of features (from AutoMatminer and SHAP analysis) and a larger set of variables, to highlight how the identification of descriptors affects the minimum number of experiments needed to pick out a MOF with the highest value of a desired property. In Fig. 1 the above procedure is schematically represented.

We highlight that sorption-based engineering applications rely upon sorbent material characterization in a wide coverage range. However, when a large number of hypothetical sorbents (here MOFs, but also zeolites in principle [50, 51]) have to be evaluated as potential candidates, only low-coverage characterization (i.e. Henry coefficient) is often accessible thus making challenging any optimization of crucial figures of merits of engineering relevance. We thus formulate an innovative procedure aiming at a fast evaluation of one of the most important figures of merit in closed water sorption seasonal thermal energy storage applications, namely the material-based specific (stored) energy. Unlike traditional sensible or latent systems [52], the above sorption based energy storage technologies have the unique advantage to be loss-free. Our procedure can thus be used in SL-based (or other) optimization/screening processes of MOFs even under incomplete knowledge of the entire isosteric field of the candidate working pairs. Applied to the database of over 5000 computationally generated (hypothetical) compounds by ref. [43] (developed for different purposes), our procedure identifies MOFs capable to largely outperform state-of-the-art sorbent materials for thermal energy storage.

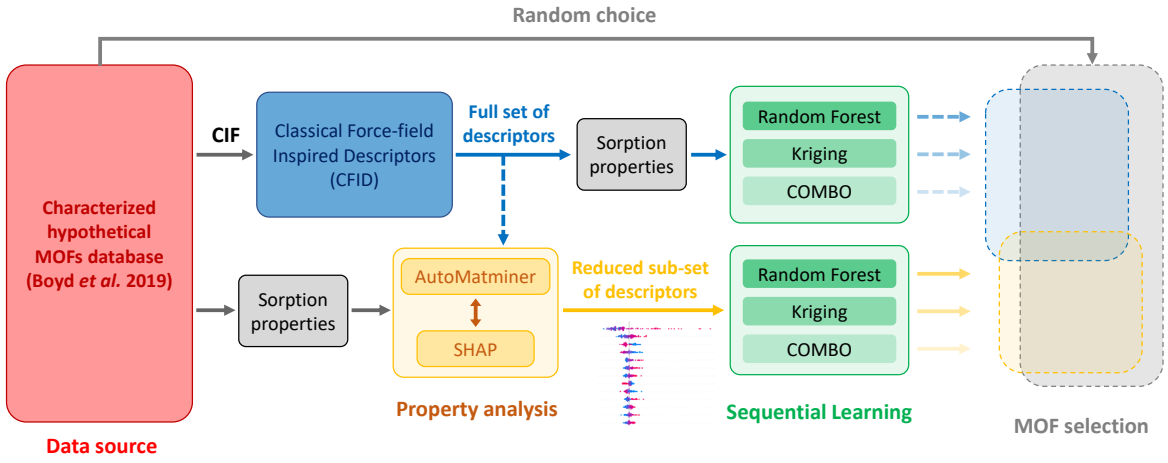


Figure 1: Overview of the methodological protocols to identify and test the minimal set of ruling crystallographic descriptors of sorption properties in several sequential learning algorithms. Over 5000 hypothetical MOFs from ref. [43] are first featurized by CFID, with the corresponding full set of descriptors provided to AutoMatminer for a preliminary descriptor reduction and machine learning models training of sorption properties of interest. The Kernel SHAP interpretation algorithm is thus used to finalize the identification and ranking of a reduced sub-set of ruling descriptors (*genetic code* of the chosen property). Several sequential learning schemes are tested using both the full set of descriptors and the reduced one for comprehensive comparison.

Results

In this work, a crucial source of data on MOFs stems from the dataset of Boyd *et al.* [43], where important sorption properties (e.g. the Henry coefficients for CO_2 and H_2O, the working capacity for CO_2, the specific surface area) have been computed by DFT-based simulations for over 8000 potential MOFs. Capitalizing on the above comprehensive study, we construct Machine Learning (ML) models

capable of accurately predicting MOFs solubility of both CO_2 and H_2O as well as CO_2 working capacity and surface area. The above models enable us to achieve the first important result of this work, namely the identification of the minimal set of crystallographic-based descriptors [53] ruling these sorption and geometric properties in MOFs.

Moreover, a systematic comparison of SL approaches on the above MOFs database reveals important conclusions on the performance of the different regression schemes adopted and, most importantly, the role played by the selection of the feature space to be explored. Those conclusions are also supported by results obtained on a highly-controllable synthetic dataset, as discussed in detail in the Supplementary Section S1.

It is worth stressing that properties reported in ref. [43] only characterize MOFs in the Henry regime and are not sufficient to describe the equilibrium sorption properties in the high coverage regime. However, when targeting important engineering applications such as seasonal thermal energy storage, key figures of merits of the storage plant (e.g. the material-based specific energy) critically rely upon the access to the entire isosteric field of the chosen sorbent-sorbate pair or, equivalently, to the knowledge of equilibrium adsorption isotherms at several temperature values [54, 55]. The latter isotherms describe the adsorption properties (at equilibrium) of sorbents in a wide range of coverage values, from the Henry regime up to the saturation pressure of the sorbate fluid.

Therefore, in this work, we also propose an innovative approach enabling us to optimize one of the most important engineering figures of merit of MOFs for seasonal thermal energy storage applications (i.e. material-based specific energy in an ideal closed sorption cycle, see Methods), even if only an incomplete set of sorption properties are (experimentally or numerically) accessible. Based on the latter optimization procedure, we are finally able to identify potential MOFs candidates for seasonal thermal energy storage that largely outperform most of the current state-of-the-art sorbent materials.

Descriptors of sorption properties in MOFs and their use in SL algorithms

We constructed four MOFs datasets, each one with the same 1557 features and a different target property among Henry coefficient for CO_2 (8194 data entries), working capacity for CO_2 (8202 data entries), Henry coefficient for H_2O (8202 data entries) and surface area (5028 data entries). The different number of data entries are due to missing values for some of the chosen properties in the available database by ref. [43].

The above database also reported, for all the compounds, both the crystallographic file (used to extract the 1557 Classical Force-Field Inspired Descriptors - CFID [44] by means of Matminer [53]), and a list of DFT-computed properties, among which we have only considered the above mentioned adsorption properties of interest. More specifically, the computed 1557 explanatory variables (also referred to as *descriptors*) proposed by Choudhary *et al.* [44] consist of a set of both chemical (e.g., average chemical properties over the elements in the cell, average atomic radial charge) and structural (e.g. distribution functions) quantities. More details on descriptor sub-categories are reported in Table 1.

Similarly to the synthetic case in Supplementary Section S1, we have trained four different ML models by means of AutoMatminer to predict the Henry coefficient for CO_2, the working capacity for CO_2, the Henry coefficient for H_2O and the surface area, achieving coefficients of determination of $R^2 = 0.803$, $R^2 = 0.655$, $R^2 = 0.885$ and $R^2 = 0.925$, respectively. We have used 80% of each dataset to train the models, and the remaining 20% to validate them. Since the Henry coefficient values span a few orders of magnitude, the corresponding ML models have been developed in terms of the natural logarithm of those properties. During the data pre-processing routines, each of the three AutoMatminer pipelines (i.e., feature reduction, data cleaning and machine learning with automatic hyper-parameter tuning, see Methods and Supplementary Section S3 for details) already drops a significant number of the 1557 features, thus confirming that many of the initially selected descriptors do not significantly affect the chosen adsorption properties. More specifically, the final models include

Table 1: Components of Classical Force-Field Inspired Descriptors (CFID) [44].

Descriptor name	**Total number**
Chemical	438
Simulation cell-size	4
Radial charge	378
Radial distribution function	100
Angular distribution up to first nearest neighbor cutoff	179
Angular distribution up to second nearest neighbor cutoff	179
Dihedral distribution up to first nearest neighbor cutoff	179
Nearest neighbor distribution	100
Total	**1557**

44 descriptors for CO_2 Henry coefficient, 92 descriptors for CO_2 working capacity, 36 descriptors for H_2O Henry coefficient and 24 descriptors for surface area.

Then, the Kernel SHAP routine [46] allows to identify the most meaningful descriptors as those accounting for the 90% of the cumulative curve over the coefficients of importance. The SHAP routine identifies the most meaningful features for the trained models among the complete set of 1557 CFID, ending up with a subset of those retained by AutoMatminer after the pre-processing. In particular, the impact of a descriptor depends on the comparison between the output of a model trained with that feature and another model output, trained without that feature (see Methods). The coefficients of importance are thus computed over the testing set, i.e., over samples the model has never encountered during the training. Since the agnostic realization of the Kernel SHAP routine is memory demanding, we have taken into account only 100 random samples from the testing set to evaluate the impact of features.

Overall, starting from the original 1557 Classical Force field Inspired Descriptors, 29 items for the CO_2 Henry coefficient, 66 for the CO_2 working capacity, 20 for the H_2O Henry coefficient and 14 for surface area are found to explain 90% of the corresponding regression models. These minimal sets of ruling descriptors are reported in Fig. 2 with the corresponding cumulative importance curves, while Figs. 3, 4, 5 and 6 show the SHAP rankings of the ten most meaningful descriptors. Table 2 summarizes the physicochemical meaning of the identified descriptors, based on the complete list by Choudhary *et al.* [44]. The list of the AutoMatminer retained variables are shown in the Supplementary Section S2, together with their cumulative importance percentage according to the SHAP rankings. As far as the four properties of MOF are concerned, the identification of those important descriptors represents *per se* an advancement of knowledge on sorption mechanism in MOFs and a first important contribution of this work.

Upon the identification of the above lists of descriptors, we have compared the performance of SL algorithms for the sorption properties of interest using both the reduced set of important descriptors (i.e. those in Figs. 3, 4 and 5) and a larger set of 100 descriptors composed by the previous and some additional (non-meaningful) ones. In particular, we have chosen the non-relevant features among the ones discarded by AutoMatminer during its automatic feature reduction procedure, before the model training. SL was adopted to find the maximum property value among a random subset of 500 samples from the original datasets (over 8000 MOFs), starting from a pool of 100 points with the lowest target property. Unexpectedly, SL optimization in the space of relevant descriptors does not ensure, in general, a faster convergence of the procedure to the optimum property value (this is also confirmed by results in the synthetic case reported in Supplementary Section S1). Furthermore, among the three regression methodologies examined, only COMBO-based methods were able to provide always a faster convergence to the optimum value as compared to the random choice strategy. Results are shown in Fig. 7.

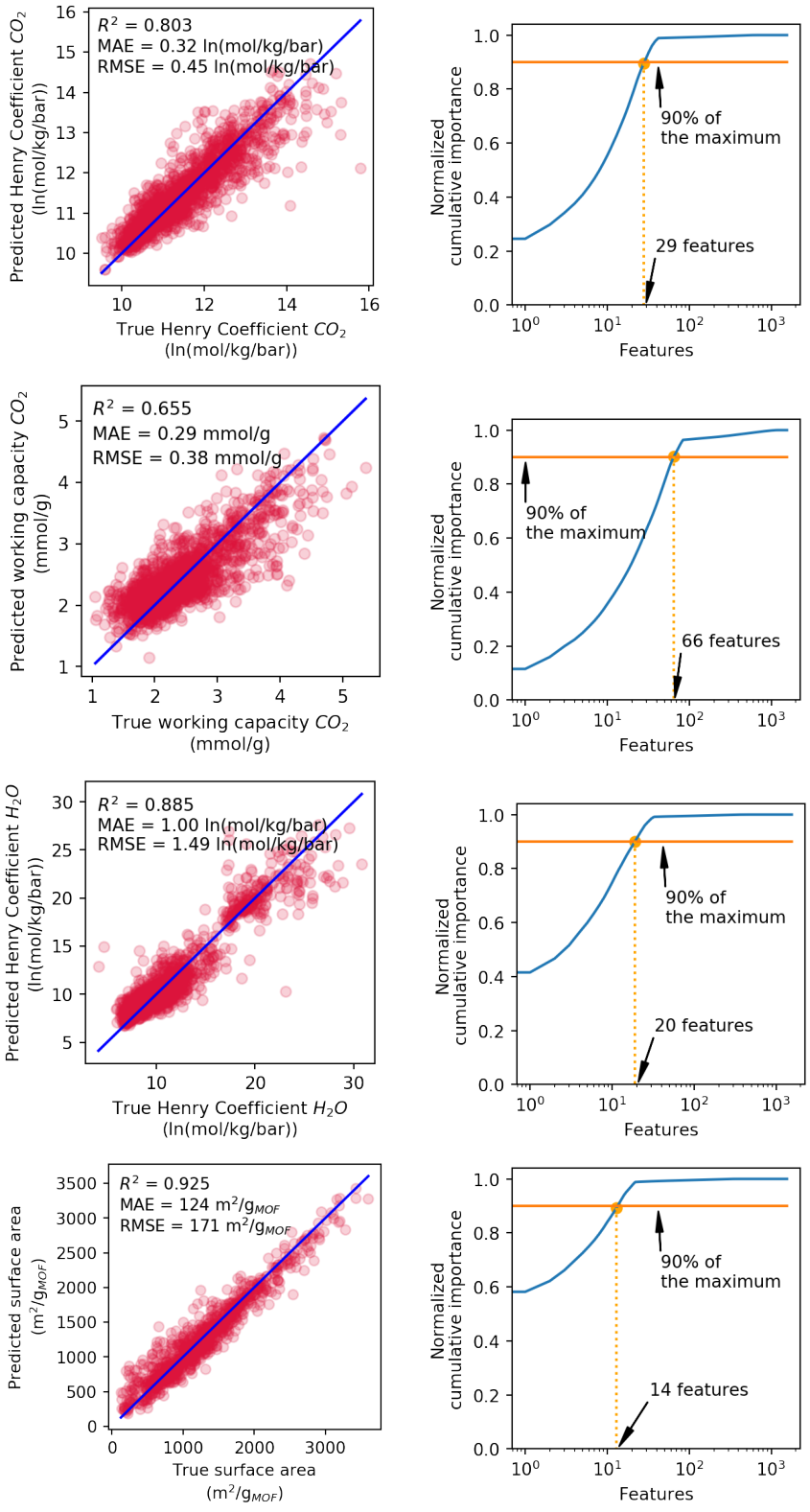


Figure 2: Predictions and corresponding normalized cumulative curves for the coefficients of importance of the four regression AutoMatminer models trained for Henry coefficient for CO_2, working capacity for CO_2, Henry coefficient for H_2O, surface area. Model performance is shown in terms of coefficient of determination R^2, Mean Absolute Error (MAE), Root Mean Squared Error (RMSE).

Table 2: Physicochemical meaning of CFID descriptors [44].

CFID descriptors	**Meaning**
'jml_jv-enp'	energy per atom of an element from JARVIS-DFT
'jml_X'	electronegativity
'jml_bp'	boiling point
'jml_mol_vol'	molar volume
'jml_atom_rad'	atomic radii
'jml_atom_mass'	atomic mass
'jml_voro_coord'	Voronoi coordination number of an elemental-crystal structure
'jml_hfus'	heat of fusion of an element
'jml_C-14'	elastic constant of the 14th element from JARVIS-DFT
'jml_polzbl'	polarizability
'jml_first_ion_en'	first ionization energy of an element
'jml_elec_aff'	electron affinity
'jml_vpa'	volume per atom of the cell
'jml_log_vpa'	logarithm of volume per atom of the cell
'jml_pack_frack'	packing fraction
'jml_mean_chg_#'	#-th descriptor of radial charge
'jml_rdf_#'	#-th descriptor of radial distribution function
'jml_adf1_#'	#-th descriptor of angular distribution up to first nearest neighbor cutoff
'jml_nn_#'	#-th descriptor of nearest neighbor distribution
'add', 'mult', 'divi'	addition, multiplication, quotient between different descriptors

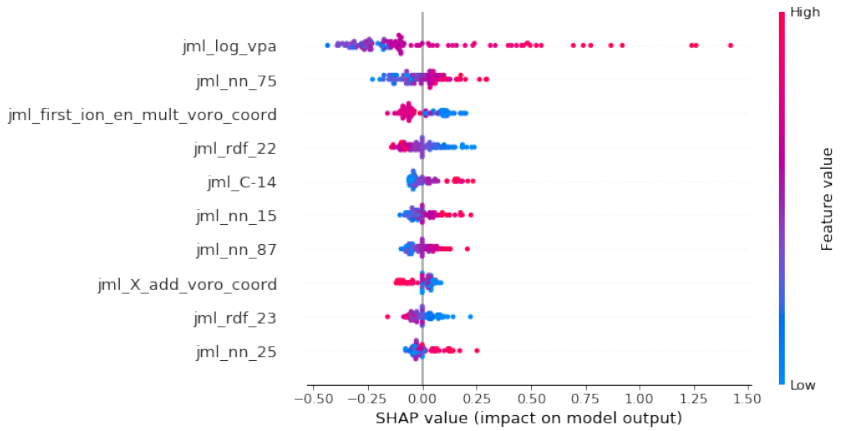


Figure 3: 10 most important features according to SHAP ranking of Henry coefficient for CO_2. For each feature (i.e., each line), 100 dots are shown, representing the 100 samples of the testing set used for computing 100 different SHAP values (impacts on the model output, horizontal axis). The color represents the corresponding feature value. The features are sorted according to the mean over the absolute SHAP values.

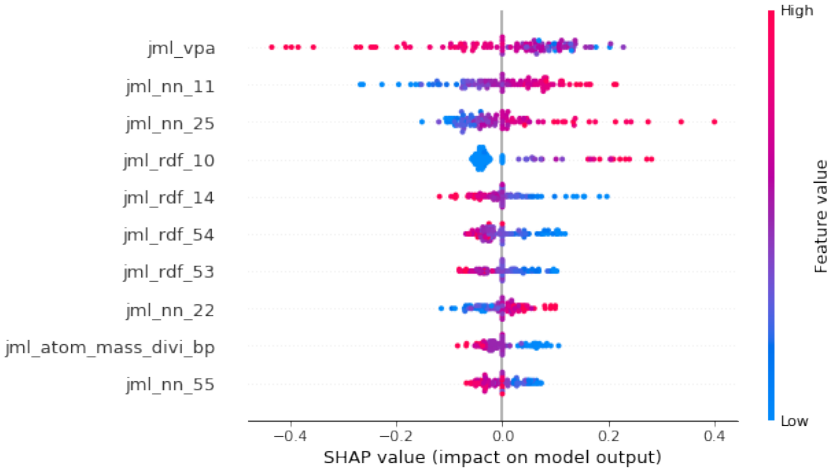


Figure 4: 10 most important features according to SHAP ranking of working capacity for CO_2. For each feature (i.e., each line), 100 dots are shown, representing the 100 samples of the testing set used for computing 100 different SHAP values (impacts on the model output, horizontal axis). The color represents the corresponding feature value. The features are sorted according to the mean over the absolute SHAP values.

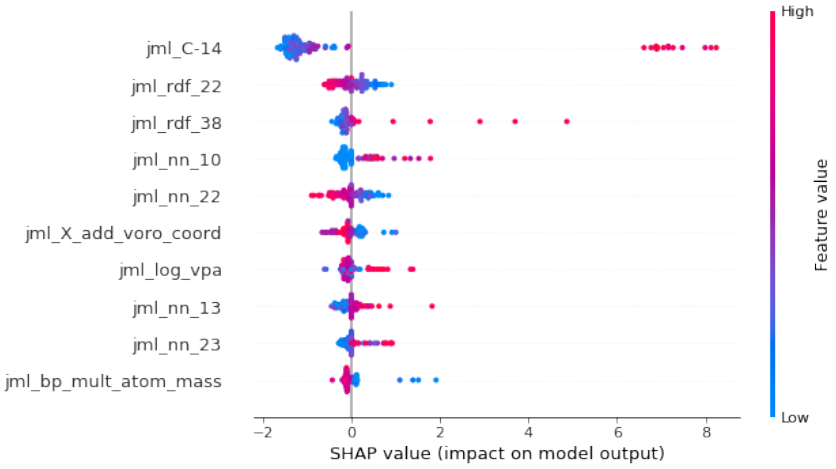


Figure 5: 10 most important features according to SHAP ranking of Henry coefficient for H_2O. For each feature (i.e., each line), 100 dots are shown, representing the 100 samples of the testing set used for computing 100 different SHAP values (impacts on the model output, horizontal axis). The color represents the corresponding feature value. The features are sorted according to the mean over the absolute SHAP values.

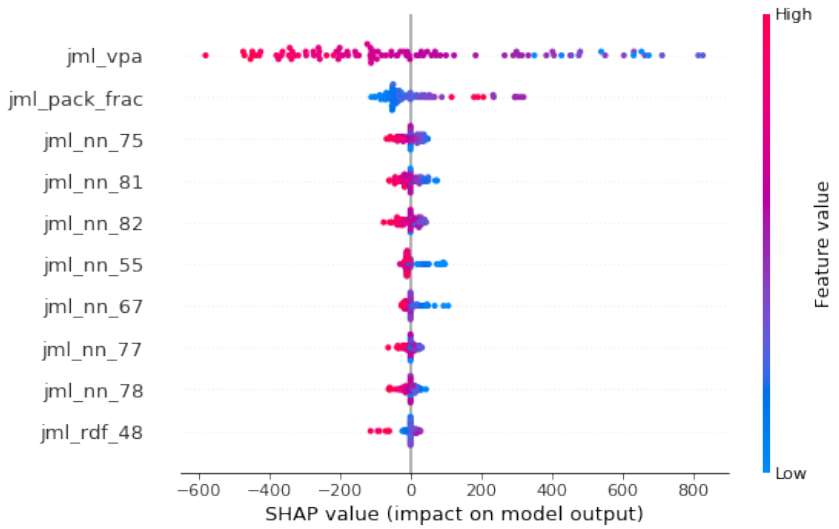


Figure 6: 10 most important features according to SHAP ranking of surface area. For each feature (i.e., each line), 100 dots are shown, representing the 100 samples of the testing set used for computing 100 different SHAP values (impacts on the model output, horizontal axis). The color represents the corresponding feature value. The features are sorted according to the mean over the absolute SHAP values.

Optimization under incomplete access to the isosteric field of candidate MOFs-water working pairs

Without losing generality, here we aim at investigating the expected performance of hypothetical (i.e. computationally generated) MOFs for an important energy engineering application, namely water-sorption seasonal thermal energy storage (see also the Methods section). The most challenging aspect of this task consists in the access to the entire isosteric field of each candidate MOF-water pair for estimating the engineering figure of merit of interest. Clearly, for a large number of MOFs candidates, this is challenging and time consuming both computationally (typically, only the Henry low-coverage regime is reported in literature works [56, 57]) and experimentally [58]. In this section, we specifically focus on such challenging aspect. We envision an efficient optimization procedure that is capable of searching MOFs with the largest expected figure of merit of engineering relevance (either by SL, if materials are sequentially synthesized/computed, or by accessing readily available databases [59]). As far as seasonal thermal energy storage applications are concerned, here we focus on the highest specific energy of MOF-water working pairs among the compounds reported in ref. [43]. An overview of the proposed methodology is schematically reported in Fig. 8.

As detailed in the Methods section, the ideal thermodynamic cycle of a closed sorption thermal energy storage system is completely defined by four operating temperatures. In this study, we assume: $T_A = 308\,\mathrm{K}$ (the minimum temperature on the user side), $T_C = 353\,\mathrm{K}$ (the maximum temperature on the source side), $T_E = 278\,\mathrm{K}$ (the average winter temperature), $T_F = 303\,\mathrm{K}$ (the average summer temperature). Those temperature values are reasonable for space heating applications in temperate climates [58]. Given the Antoine equation, the equilibrium water vapour pressures $p_E = 866.2\,\mathrm{Pa}$ at the evaporator and $p_F = 4231.6\,\mathrm{Pa}$ at the condenser are also uniquely defined considering the average winter and summer temperatures, respectively. We decided to evaluate and maximize over the database one the most important engineering quantities in a thermal energy storage plant, namely the cycled heat per unit of material weight. While full details on the adopted models are given in the Methods section, in the following we report and discuss the main simplifying assumptions in our approach:

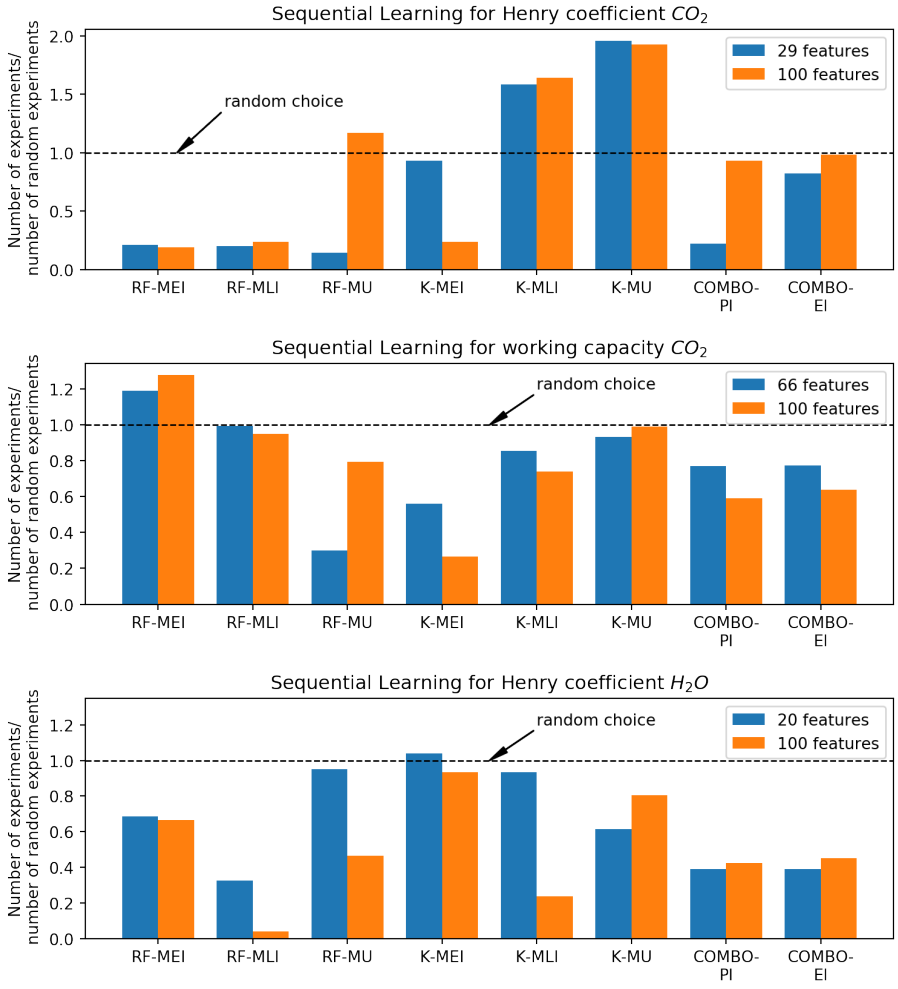


Figure 7: Number of evaluations before converging to the maximum for the SL algorithms, normalized with respect to the random choice (corresponding to 200 experiments), for three sorption properties of MOFs: Henry coefficient for CO_2, working capacity for CO_2, Henry coefficient for H_2O. The initial set consists of the same worst 100 candidates (in terms of the target property) from a random subset of 500 samples of the original database.

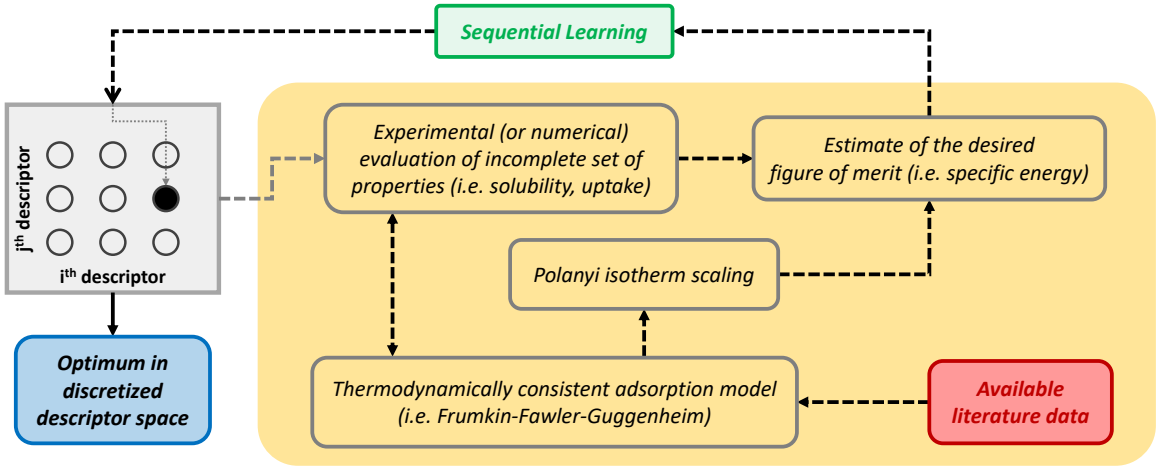


Figure 8: Suggested procedure for estimating the specific energy of hypothetical MOF-water working pairs when only an incomplete knowledge of the isosteric field is experimentally or numerically accessible (highlighted in yellow).

- A key quantity to be estimated is the H_2O working capacity. That quantity is related to the available adsorption sites n_{TOT} per unit of dry sorbent mass. Boyd *et al.* [43] reported only the CO_2 working capacity, while no data are available on the maximum H_2O uptake. Nonetheless, we can rely on other related properties, such as the specific surface area of MOD. To this end, we notice that Chaemchuen *et al.* have reported H_2O working capacity for a pool of 66 MOFs [5]. A good correlation between the water uptake and the surface area (i.e., the available internal surface per gram of dry adsorbent) can be observed for typical MOFs used in the energy engineering field. On the basis of that correlation, we impose a linear regression for finding the constant of proportionality between water uptake and surface area (water uptake $= \eta \times$ surface area). This yields $\eta = 3.875 \times 10^{-4}\,\mathrm{g_{H_2O}/m^2}$. More details can be found in Supplementary Section S4.

- Henry coefficients $\widetilde{H}(T_0)$ for H_2O are listed at the reference temperature $T_0 = 298\,\mathrm{K}$ with units of $\mathrm{mol_{H_2O}/kg_{MOF}/bar}$, thus representing the moles of adsorbed H_2O per kilogram of dry MOF per bar of H_2O vapour. In our approach, we adopt the Frumkin-Fawler-Guggenheim (FFG) model to estimate the adsorption isotherm over the entire range of coverages only relying upon such Henry coefficient. However, as discussed in the Methods sections, the FFG equation requires $H(T_0)$ in units of $\mathrm{Pa^{-1}}$: we have thus converted $\widetilde{H}(T_0)$ (readily available from ref. [43]) to $H(T_0)$. Let n_s, m_{MOF} and p_{H_2O} be the number of adsorbed water moles, the mass of the potential MOF and the pressure of water in vapour phase, respectively, it holds:

$$\widetilde{H}(T_0) = \frac{n_s}{m_{MOF} p_{H_2O}}. \tag{1}$$

  The approximation of low-coverage regime yields the linear relationship between the coverage and pressure, namely $\theta = H(T_0) p_{H_2O}$. Since the number of adsorbed water moles is related to the molar based total number of adsorption sites as $n_s = \theta n_{TOT}$, it follows:

$$H(T_0) = \widetilde{H}(T_0) \frac{\mathcal{M}_{MOF}}{n_{TOT}/n_{MOF}}, \tag{2}$$

  with $m_{MOF} = \mathcal{M}_{MOF} n_{MOF}$, $\mathcal{M}_{MOF}$ the molecular weight of the MOF, and n_{MOF} the total number of moles. Furthermore, the molar based total number of adsorption sites n_{TOT} corresponds to the maximum number of water moles n_{MAX,H_2O} that can be adsorbed, and the

following relationship holds:

$$\frac{n_{MAX,\mathrm{H_2O}}}{n_{MOF}} = \frac{m_{MAX,\mathrm{H_2O}}}{m_{MOF}} \frac{\mathcal{M}_{MOF}}{\mathcal{M}_{\mathrm{H_2O}}}, \tag{3}$$

where $\mathcal{M}_{\mathrm{H_2O}}$ is the molecular weight of water and $m_{MAX,\mathrm{H_2O}}$ denotes the maximum mass of water that can be adsorbed. The ratio $m_{MAX,\mathrm{H_2O}}/m_{MOF}$ is related to the H_2O working capacity of the MOF and it is equal to ηS, where η is the constant of proportionality between the uptake and the surface area S. A comparison of Eq. 3 and Eq. 2 yields:

$$H(T_0) = \widetilde{H}(T_0) \frac{\mathcal{M}_{\mathrm{H_2O}}}{\eta S} \times 10^{-8}, \tag{4}$$

which is the final conversion formula of the Henry coefficient for H_2O from measure units of $\mathrm{mol_{H_2O}\,kg^{-1}_{MOF}\,bar^{-1}}$ into $\mathrm{Pa^{-1}}$. Here, the factor 10^{-8} appears because $[\mathcal{M}_{\mathrm{H_2O}}] = \mathrm{g_{H_2O}/mol_{H2O}}$, $[\eta] = \mathrm{g_{H_2O}/m^2}$, $[S] = \mathrm{m^2/g_{MOF}}$, and so $[\widetilde{H}(T_0)\mathcal{M}_{\mathrm{H_2O}}/(\eta S)] = \mathrm{g_{MOF}\,kg^{-1}_{MOF}\,bar^{-1}}$.

- A crucial quantity for heat transformation is the isosteric heat of adsorption q_{st}. Due to the Clausius-Clapeyron relationship (see eq. 7 in the Methods section), at least two adsorption isotherm curves (at T_A and at T_C) are needed to estimate the corresponding q_{st}. In our database, though, the Henry coefficients are only available at T_0. In order to reconstruct a second adsorption isotherm for the same MOF-water working pair, we decided to resort to the potential theory of Polanyi, thus exploiting the basic notion that all adsorption isotherms are self-similar when rescaled with respect to the Polanyi potential function. Details are provided in the Supplementary Section S5. More specifically, the Polanyi potential is defined as:

$$\mathcal{A} = -RT \ln\left(\frac{p_s(T)}{p}\right), \tag{5}$$

where $p_s(T)$ is the saturation pressure of water at temperature T, while p is the pressure of the vapour phase on the adsorbent surface [60]. Since, at a given pressure p, the Polanyi potential is a constant of the sorption pair, we have computed $\mathcal{A}$ at T_0 in a range from 10^{-4} Pa up to $p_s(T_0) = 3157$ Pa (Antoine equation for water); then, in the $\theta - p$ chart, we have rescaled the abscissa p of the isotherm obtained at the temperature T_0 according to $p = p_s(T)\exp(\mathcal{A}/(RT))$, for getting the new curves at T_A and T_C. We have finally computed the isosteric heat by means of the Clausius-Clapeyron relationship:

$$q_{st} = \frac{R}{3} \frac{T_C T_A}{T_C - T_A} \sum_{i=1}^{3} \ln \frac{p_2(\theta_i)}{p_1(\theta_i)}, \tag{6}$$

where the points 1 and 2 represent the intersections of an isosteric transformation with the two isotherms respectively at T_A and T_C. We have repeated the procedure for three coverage values (i.e. $\theta_1 = 0.4$, $\theta_2 = 0.5$, $\theta_3 = 0.6$) and averaged them.

- Finally, upon determination of the low- and high-temperature adsorption isotherms curves at T_A and T_C, the coverage span $\Delta\theta$ during the discharge phase can be determined as detailed in the Methods section. As for the estimate of the isosteric heat, this requires for all the compounds the rescaling of the horizontal axis in the $\theta - p$ chart of the isotherm obtained at temperature T_0 according to the Polanyi potential theory.

We have thus computed the following objective function $Sq_{st}\Delta\theta$, which recovers the cycled heat up to a constant, over the entire list of 5028 potential MOFs with positive surface area in ref. [43]. The best MOF turned out to be the compound with chemical formula $C_{96}H_{48}O_{28}N_8V_4$ and referred to as "str_m5_o18_o28_sra_sym.72" in the database (see also the molecular rendering in Fig. 9), with Henry

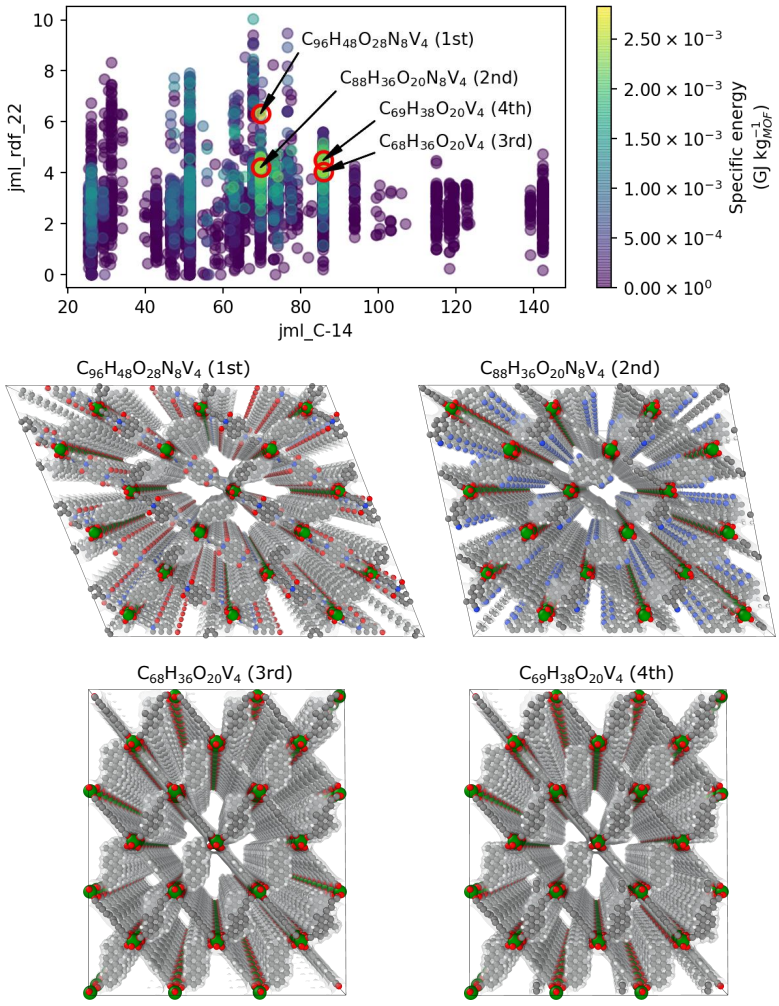


Figure 9: The entire set of 5028 potential MOFs in the database by Boyd *et al.* [43] is displayed in the 2D chart, where the first two SHAP ranked descriptors for the H_2O Henry coefficient are represented. The best four MOFs sorbents for the adsorption/desorption based thermal storage application are highlighted in the 2D chart, and 3x3x13 replications of the respective crystallographic cells depicted (C atoms: gray; H atoms: white; O atoms: red; N atoms: blue; V atoms: green).

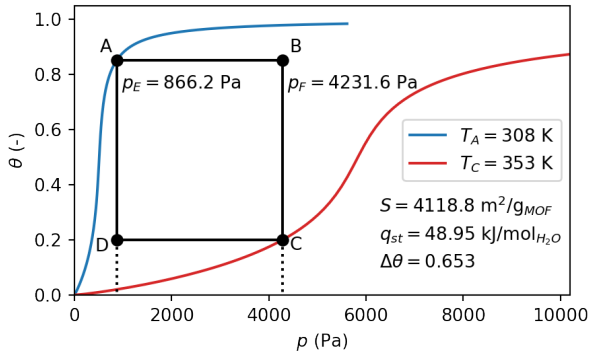


Figure 10: Adsorption/desorption based thermal energy storage cycle for the potential MOF "str_m5_o18_o28_sra_sym.72" with water, in the coverage-pressure plane. The isotherms $T_A = 308\,\mathrm{K}$ and $T_C = 353\,\mathrm{K}$ are shown. Surface S, isosteric heat q_{st}, and coverage span $\Delta\theta$ over the cycle are reported, giving an objective function $Sq_{st}\Delta\theta = 1.32 \times 10^5\,\mathrm{kJ\,m^2\,mol^{-1}_{H_2O}\,g^{-1}_{MOF}}$ or equivalently $2.83 \times 10^{-3}\,\mathrm{GJ/kg_{MOF}}$, which corresponds to $1.73\,\mathrm{GJ/m^3}$.

coefficient at 298 K of $6110.54\,\mathrm{mol_{H_2O}\,kg^{-1}_{MOF}\,bar^{-1}}$ (or equivalently, $6.89 \times 10^{-4}\,\mathrm{Pa^{-1}}$) and surface area $S = 4118.79\,\mathrm{m^2/g_{MOF}}$. Figure 10 shows also the ideal expected thermodynamic cycle related to this optimal potential MOF.

We observe a coverage span $\Delta\theta = 0.653$, an isosteric heat $q_{st} = 48.95\,\mathrm{kJ/mol_{H_2O}}$ with an objective function value of $1.32 \times 10^5\,\mathrm{kJ\,m^2\,mol^{-1}_{H_2O}\,g^{-1}_{MOF}}$. That quantity can be directly related to specific energy: upon multiplication by the constant $\eta/\mathcal{M}_{\mathrm{H_2O}}$ ($\eta = 3.875 \times 10^{-4}\,\mathrm{g_{H_2O}/m^2}$, $\mathcal{M}_{\mathrm{H_2O}} = 18.02\,\mathrm{g_{H_2O}/mol_{H_2O}}$), we obtain a value of $2.83 \times 10^{-3}\,\mathrm{GJ/kg_{MOF}}$. Furthermore, we can compute the theoretical density ρ_{MOF} of the crystal knowing the mass of the cell ($1965.21\,\mathrm{u} = 3.263 \times 10^{-21}\,\mathrm{g_{MOF}}$, as from the database) and its volume ($5.335 \times 10^{-21}\,\mathrm{cm^3}$, as from the CIF file), leading to $\rho_{MOF} = 0.612\,\mathrm{g_{MOF}/cm^3}$. As a result, the volume-based energy density turns out to be $1.73\,\mathrm{GJ/m^3}$. For the sake of comparison, Fig. 9 shows a 2D map where the two axes represent the two most important descriptors according to the SHAP ranking for the Henry coefficient of H_2O: the four top performing potential MOFs are highlighted and the corresponding crystallographic cells depicted. Moreover, Table 3 shows the ten most performing potential MOFs ranked in terms of specific energy.

As depicted in Fig. 11, the four top performing potential MOFs show (material based) specific energy values among the highest available in the literature for sorption thermal energy storage under similar operating conditions.

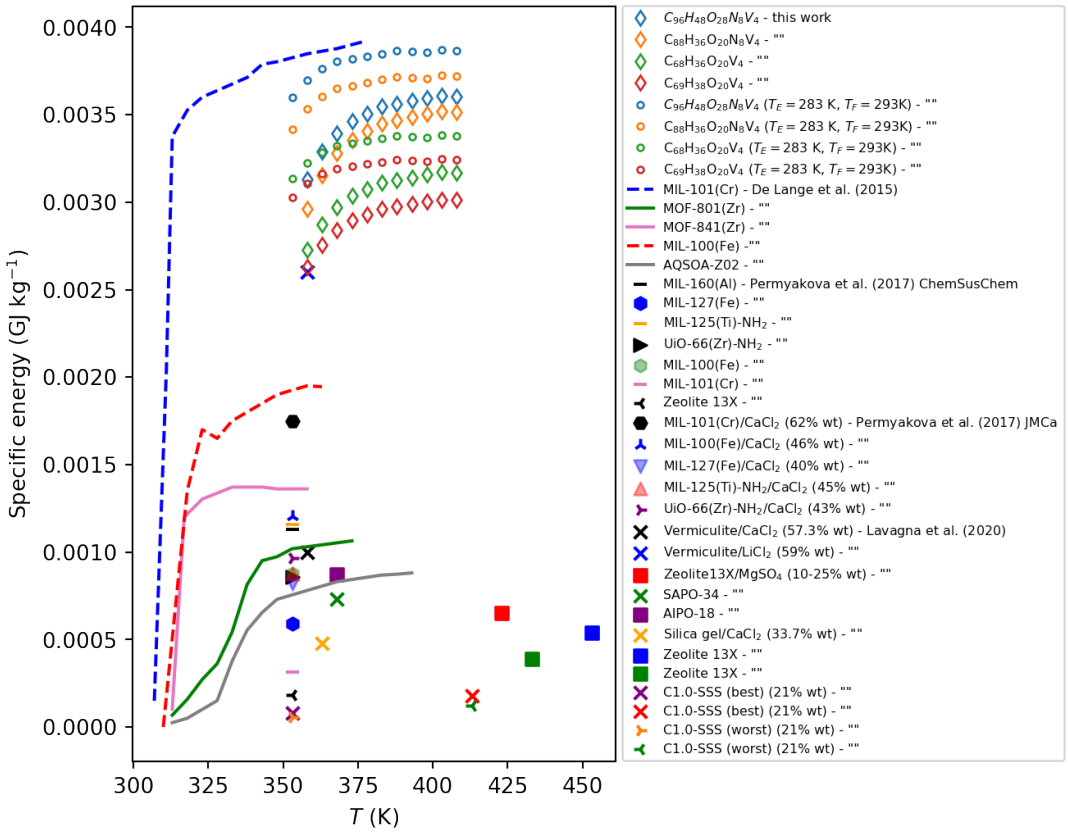


Figure 11: Comparison between the expected specific energy for different desorption temperatures of the optimum MOFs identified in this work (either standard environmental conditions, i.e. evaporation temperature $T_E = 278\,\mathrm{K}$ and condensation temperature $T_F = 303\,\mathrm{K}$, or with conditions of $T_E = 283\,\mathrm{K}$ and $T_F = 293\,\mathrm{K}$) and several water sorbent materials reported in the literature.

Table 3: Top ten potential MOFs in terms of specific stored energy from the database by Boyd *et al.* [43]. The name indicated in the database, the brute formula, the molecular weight, the surface area and the specific energy are shown.

Database name	Brute formula	Molecular weight (u)	Surface area (m^2/g_{MOF})	Specific energy ($\times 10^{-3}$ GJ/kg_{MOF})
"str_m5_o18_o28_sra_sym.72"	$C_{96}H_{48}O_{28}N_8V_4$	1965.21	4118.79	2.83
"str_m5_o3_o18_sra_sym.73"	$C_{88}H_{36}O_{20}N_8V_4$	1729.03	3888.89	2.57
"str_m5_o6_o18_sra_sym.82"	$C_{68}H_{36}O_{20}V_4$	1376.76	3577.31	2.44
"str_m5_o6_o18_sra_sym.92"	$C_{69}H_{38}O_{20}V_4$	1390.79	3473.55	2.40
"str_m5_o7_o18_sra_sym.115"	$C_{76}H_{32}O_{20}N_4V_4$	1524.85	3428.98	2.36
"str_m5_o7_o18_sra_sym.133"	$C_{72}H_{36}O_{28}V_4$	1552.81	3384.12	2.34
"str_m5_o7_o18_sra_sym.136"	$C_{72}H_{40}O_{20}N_4V_4$	1484.87	3362.19	2.31
"str_m5_o7_o18_sra_sym.20"	$C_{76}H_{36}O_{24}V_4$	1536.85	3340.13	2.22
"str_m5_o7_o18_sra_sym.124"	$C_{72}H_{40}O_{20}N_4V_4$	1484.87	3355.61	2.22
"str_m5_o6_o18_sra_sym.17"	$C_{70}H_{40}O_{19}V_4$	1404.82	3189.28	2.22

Discussion

Sequential Learning (SL) algorithms can in principle dramatically reduce the number of evaluations needed for finding the optimum of an unknown function as compared with a naive random choice and, as such, they are emerging as effective tools for material optimization and discovery. In this work, focusing on Metal Organic Frameworks - MOFs and some of their crucial adsorption properties (both with H_2O and CO_2 as sorbate fluids), we have addressed a number of critical aspects related to the discovery of the minimal set of important crystallographic descriptors for SL based optimization algorithms. We have shown that the general protocol for sorting out the minimal set of ruling descriptors (here referred to as crystallographic *genetic code*) for a given adsorption property is based on two steps: i) construction and training of Machine Learning (ML) model which identifies the number of ruling descriptors; ii) evaluation of the relative importance of each explanatory variable on the chosen output by the SHAP analysis. We found that, as long as the set of such ruling descriptors (for a given property of interest) is included among the exploration space features, convergence performance is not affected, although the computational burden of a SL algorithm also depends on the dimension of the parameter space to be explored: taking into account only the most relevant features may be in fact beneficial in that respect. Furthermore, based on the several examples provided here (i.e. Henry coefficient for CO_2, Henry coefficient for H_2O, working capacity for CO_2 as well as the synthetic example discussed in the Supplementary Section S1), we have consistently noticed that only the COMBO algorithms always perform better than random guessing.

Furthermore, we recognize that full access to the adsorption properties of hypothetical MOFs in the entire coverage regime (as requested in important applications of engineering relevance) is very challenging both experimentally and computationally. This holds particularly for water-MOFs working pairs that are promising for a number of energy applications. Hence, we formulate an innovative, general and efficient computational screening of hypothetical MOFs which, only relying upon the adsorption properties reported in Fig. 2, is capable to estimate important figures of merit for sorption based seasonal thermal energy storage. Remarkably, our procedure suggests that some of the MOFs hypothesized in the database by ref. [43] (developed for completely different purposes) are expected to largely outperform most of the state-of-the-art water sorbent compounds. We believe that the above results represent a first important step towards efficient MOFs screening and optimization, not only with respect to intrinsic materials properties but also (and importantly) with respect to figures of merit of engineering relevance for applications such as thermally driven water harvesting from air, water sorption thermal energy storage, and solar cooling.

Clearly, our approach is based on a number of approximations and it still requires additional research activities, that are currently ongoing. First, we notice that a large set of hypothetical MOFs may be characterized by properties (e.g. Henry coefficients) whose values span several orders of magnitude. Hence a unique ML model, as used in this pipeline, may achieve a high coefficient of determination if its logarithm is considered. Nonetheless, the computation of the coverage span $\Delta\theta$ depends directly on the Henry coefficient, which may thus be affected by a relatively high error. Furthermore, additional simplifying assumptions that have been used in our approach include fixed parameters such as the constant of proportionality between the specific surface area and the water working capacity, as well as the *steepness* coefficient β in the FFG model. Without loosing generality, those assumptions could be relaxed in the near future relying on more sophisticated models. One possible way to tackle those challenges (not necessarily the only possible strategy) may be a preliminary classification of the hypothetical MOFs based on properly trained ML classifiers, with the purpose of assigning a given compound of interest to a specific category (e.g. the set of MOFs with Henry coefficient of similar magnitude, similar β, etc.), then providing property predictions on each MOF category.

Methods

Water sorption thermal energy storage

In this work we focus on the use of potential MOFs for water-sorption based thermal storage applications. Physical adsorption processes are based on weak and reversible interactions between the (solid) sorbent material and the corresponding adsorbate, i.e. the fluid [61]. Those phenomena are relevant to thermal energy engineering as sorption/desorption in solid sorbents can be accompanied by significant amount of energy exchange. In the following, the solid sorbent are MOFs, while water is the adsorbate.

To allow desorption of an infinitesimal number ($\mathrm{d}n$) of moles of adsorbate from the adsorbent surface, a given amount of heat $\mathrm{d}Q = q_{st}\,\mathrm{d}n$ has to be provided to the system, where q_{st} (with units of kJ/mol) denotes the isosteric heat. Since the process is reversible, the same amount of heat $\mathrm{d}Q$ is released by the dry sorbent when $\mathrm{d}n$ moles of fluid at a pressure p, initially in vapour phase, are adsorbed. Furthermore, we define the load X as the ratio between the mass of adsorbate and the mass of dry sorbent. A process characterized by constant load X is referred to as an *isosteric transformation* and the popular Clausius-Clapeyron relationship yields:

$$\left(\frac{\partial \ln p}{\partial\left(-\frac{1}{T}\right)}\right)_X = \frac{q_{st}}{R}, \tag{7}$$

where T is the absolute temperature and $R = 8.314\,\mathrm{J\,mol^{-1}\,K^{-1}}$ denotes the gas constant [62]. Therefore, an isosteric transformation in the Clapeyron chart ($\ln p$ vs $-1/T$) is a curve with local slope q_{st}/R. Similarly, the adsorbate isosteric curve has a slope $\Delta H_{(vap)}/R$, where $\Delta H_{(vap)}$ is the molar enthalpy for liquid-vapour phase change of the adsorbate.

Closely related to the load X, the coverage θ is defined as the ratio between the number of already occupied adsorption sites n_s and the total available number of sites n_{TOT}. At equilibrium and at a given temperature T, the coverage θ depends on the pressure p of the vapour phase according to an adsorption isotherm, whose shape depends on the sorbent/adsorbate pair. MOFs/water pairs are known to show typical "S-shaped" isotherms in the $\theta - p$ chart (i.e. type V of the IUPAC classification [63]). Thus, in the following, we make the assumption that the Frumkin-Fawler-Guggenheim (FFG) model can be used conveniently for describing analytically the MOFs-water adsorption isotherms:

$$\theta = \frac{H(T)p\exp\left(\beta\theta\right)}{1 + H(T)p\exp\left(\beta\theta\right)}, \tag{8}$$

where $\beta = \frac{\overline{n}E_p}{RT}$ rules the *steepness* of the "S-shape", $\overline{n}$ denotes the neighboring binding sites and E_p represents the additional binding energy due to lateral interactions [60]. We have used the FFG model to interpret eight experimental isotherms of real MOF-water pairs and achieve a proper choice of β. In particular, for each curve, we have identified the best value of β in terms of a least squares approach; then, we have taken the mean over those 8 values, ending up with $\beta = 3.4$. More details can be found in the Supplementary Section S6. Finally, $H(T)$ is the Henry coefficient for the specific sorbent/adsorbate pair (with units $\mathrm{Pa^{-1}}$) at a given absolute temperature T.

A schematic of a closed water sorption thermal energy storage system is shown in Fig. 12. These systems are based on a reactor, containing the solid sorbent, connected with a condenser/evaporator by means of a valve [54]. This chemical apparatus follows a seasonal closed cycle completely defined by four temperatures: T_A (the minimum temperature on the user side), T_C (the maximum temperature on the source side), T_E (the average winter temperature), T_F (the average summer temperature). The two pressures p_E (evaporator) and p_F (condenser) are related to the absolute temperatures T_E and T_F, respectively, through the Antoine equation for water saturation $p_{E,F} = 133.2 \times 10^{A-B/(C+T_{E,F}-273)}$, where $A = 8.07131$, $B = 1730.63$, $C = 233.426$ [64]. Hence, the ideal thermodynamic cycle of a closed thermal energy storage process (see Fig. 13) is based on the following four steps:

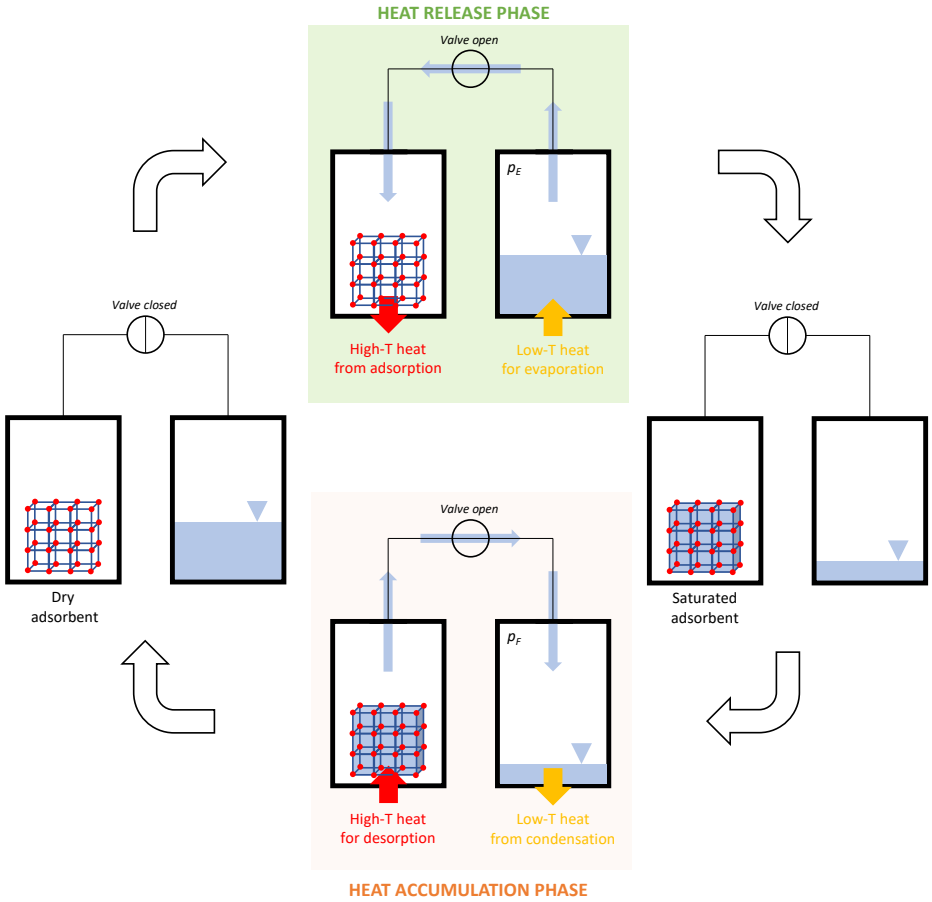


Figure 12: Schematic of a closed water sorption thermal energy storage system, in which the cycle underlying the heat accumulation and successive release is represented.

1. The sorbent/adsorbate is heated isosterically up to a temperature T_B, corresponding to a pressure p_F in the condenser (line AB).

2. Heating of the pair continues at constant pressure p_F and desorbed vapour flows to the condenser through the opened valve. In the condenser, the adsorbate rejects the condensation heat into the environment while condensing until the maximum temperature of the heat source T_C is reached (line BC). The condition of minimum load is reached and the valve gets closed.

3. Keeping the valve closed, the system in contact with the environmental temperature cools isosterically during the storage period (line CD) down to temperature T_D, corresponding to the evaporator pressure p_E.

4. During the discharge phase of the heat storage system, the valve is opened to let the adsorbate evaporate and reach the reactor. During this isobaric transformation (line DA), the heat of adsorption Q_{DA}, also known as cycled heat, is released.

One of the most important figures of merit for energy storage systems is the volumetric energy density, namely the maximum energy that can be stored per unit of volume of the plant [65]. Clearly, at fixed plant size, the higher the cycled heat the higher the volumetric energy density of the storage system. In this view, the choice of the solid sorbent material for a given adsorbate is key for maximizing

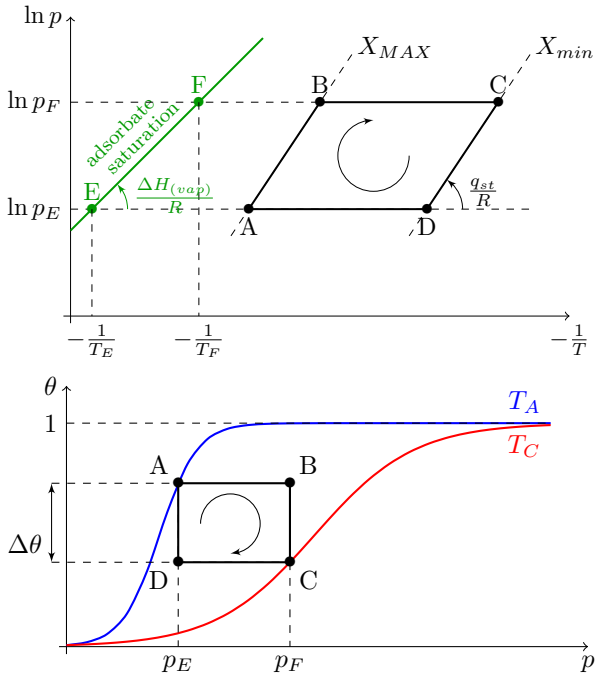


Figure 13: Schematics of ideal adsorption/desorption thermal energy storage cycle. Top: Ideal cycle in the Clapeyron chart. Bottom: Same ideal cycle in the coverage-pressure chart, between the two limiting isotherms passing by $\theta(p, T_A)$ and $\theta(p, T_C)$.

the cycled heat in the ideal thermodynamic cycle and therefore the expected volumetric energy density. We thus perform below a material screening aiming at the maximum value of the following cycled heat (i.e., the released heat during the DA process in Fig. 13):

$$Q_{DA} = \int_D^A q_{st}\,\mathrm{d}n_s = \int_D^A n_{TOT} q_{st}\,\mathrm{d}\theta \approx n_{TOT} q_{st} \Delta\theta, \tag{9}$$

where we have used the definition of heat of adsorption $\mathrm{d}Q = q_{st}\,\mathrm{d}n_s$, coverage $\theta = n_s/n_{TOT}$ and the approximation $q_{st} \approx$ const.

Sequential Learning

Typical steps in any SL algorithm consist in (i) constructing a regression model over known data, (ii) using a strategy to suggest the best-unmeasured point to test, (iii) enlarging the known dataset with this tested point and (iv) iterating up to the tested candidate meets the needed specification. Let $\mathcal{D} = \{(\mathbf{x}_1, y_1), \ldots, (\mathbf{x}_n, y_n)\}$ denotes a set of n training data, where $\mathbf{x}_i \in \mathbb{R}^d$ and $y_i \in \mathbb{R}$ represent the i-th vector of descriptors and its known response, respectively. Let $\{\mathbf{x}_{n+1}, \ldots, \mathbf{x}_m\}$ denote the $m - n$ d-dimensional arrays of descriptors with unknown responses $\{y_{n+1}, \ldots, y_m\}$. To find the location $\mathbf{x}^*$ of the maximum y^*, we would need the exact model $y = f(\mathbf{x})$. However, given the restricted set $\mathcal{D}$ of training data, only a surrogate model $y = \hat{f}(\mathbf{x}|\mathcal{D})$ can be constructed. Hence, for each unmeasured point $i = n + 1, \ldots, m$, different regression methodologies (here FUELS-Random Forest, kriging and COMBO-Gaussian processes) can be used to estimate the response $\hat{f}(\mathbf{x}_i)$ in terms of a mean value $\mu(\mathbf{x}_i)$ and the corresponding uncertainty $\sigma(\mathbf{x}_i)$, indicating the robustness of the prediction. To measure the performance of any combination *regression model/query strategy*, we put ourselves in the practitioner's perspective, who is interested in a unique sequence of points to be tested, and not in an average over more paths (as, for instance, shown in ref. [47]). To achieve this, for those regression models not

allowing a deterministic prediction (i.e., Random Forest and COMBO), at each step we have repeated 100 times the choice of the next point to query, picking the most preferred one. A comprehensive comparison of the above methodologies is reported in the results, and the complete details on the adopted algorithms can be found in the Supplementary Sections S7 and S8.

Model training and choice of the descriptors

The first issue to be addressed when applying SL to material optimization is computation and selection of relevant features (or descriptors). The descriptor issue is critical in materials science [66, 67] as well as in other computational fields [68]. In this work, we first investigate to which extent the choice of a minimal set of relevant descriptors is critical for the fast convergence of SL algorithms.

To this end, before even implementing SL procedures, we decided to perform a preliminary feature *pruning* for discovering the most meaningful ones in terms of the target property. We use the entire dataset (both descriptors and target property) to train and validate a regression model by means of AutoMatminer [45], which allows to automatically train and validate a complete pipeline - feature reduction, data cleaning and machine learning - with automatic hyper-parameter tuning. In particular, AutoMatminer contains a customized dictionary of operators in terms of feature preprocessors, feature selectors and ML models. The algorithm automatically searches for their best combination, with the best ML model hyperparameters. Specifically, we have removed some of the default operators from the AutoMatminer proposed list, in order to have a stable code (e.g., to avoid the drop of all the features in the preprocessing step). The list of the retained ones can be found in the Supplementary Section S3. The degree of accuracy and the training time depend on the choice of the predefined set of options, which specify how the search of the best pipeline works. We choose the preset "express" for a synthetic dataset (moderate accuracy and relatively quick training), and the preset "production" for the effective MOFs datasets (higher accuracy and slower training). Upon model training and validation, we detect the most important features thanks to the Kernel SHAP algorithm in its model agnostic realization [46], thus quantifying to which extent a given feature impacts on the output. The latter methodology is based on the classical Shapley value, which has in game theory its original field of application. There, the problem of assigning, in a cooperative game, a proportional reward to each player is addressed based on the real contribution provided to the common objective of the coalition. In a model, given F the set of all features and its generic subset $S \subseteq F$, the importance of the $i-$th descriptor depends on the comparison between the model $f_{S\cup\{i\}}$ trained with that explanatory variable, and another model f_S trained without that feature; then, the difference between the predictions $f_{S\cup\{i\}}(\mathbf{x}_{S\cup\{i\}}) - f_S(\mathbf{x}_S)$ is computed, where $\mathbf{x}_{S\cup\{i\}}$ and $\mathbf{x}_S$ represent respectively the values of the input features over the subsets $S\cup\{i\}$ and S. This difference is weighted over all possible subsets S and the importance value of the $i-$th feature turns out to be

$$\phi_i = \sum_{S\subseteq F\setminus\{i\}} \frac{|S|!(|F|-|S|-1)!}{|F|!}\left(f_{S\cup\{i\}}(\mathbf{x}_{S\cup\{i\}}) - f_S(\mathbf{x}_S)\right), \tag{10}$$

where $|\cdot|$ denotes the number of elements. Because of the huge number of possible descriptors subsets S of a set F, the classical Shapley values of Eq. 10 are computationally challenging: therefore, the SHAP package provides suitable approximations.

Data availability

The data that support the findings of this study are available from the corresponding author upon reasonable request.

Code availability

Upon request to the corresponding Author.

References

[1] S. Kitagawa *et al.*, "Metal–organic frameworks (mofs)," *Chemical Society Reviews*, vol. 43, no. 16, pp. 5415–5418, 2014.

[2] K. Adil, Y. Belmabkhout, R. S. Pillai, A. Cadiau, P. M. Bhatt, A. H. Assen, G. Maurin, and M. Eddaoudi, "Gas/vapour separation using ultra-microporous metal–organic frameworks: insights into the structure/separation relationship," *Chemical Society Reviews*, vol. 46, no. 11, pp. 3402–3430, 2017.

[3] S. M. Rogge, A. Bavykina, J. Hajek, H. Garcia, A. I. Olivos-Suarez, A. Sepúlveda-Escribano, A. Vimont, G. Clet, P. Bazin, F. Kapteijn, *et al.*, "Metal–organic and covalent organic frameworks as single-site catalysts," *Chemical Society Reviews*, vol. 46, no. 11, pp. 3134–3184, 2017.

[4] S. Wuttke, M. Lismont, A. Escudero, B. Rungtaweevoranit, and W. J. Parak, "Positioning metal-organic framework nanoparticles within the context of drug delivery–a comparison with mesoporous silica nanoparticles and dendrimers," *Biomaterials*, vol. 123, pp. 172–183, 2017.

[5] S. Chaemchuen, X. Xiao, N. Klomkliang, M. S. Yusubov, and F. Verpoort, "Tunable metal–organic frameworks for heat transformation applications," *Nanomaterials*, vol. 8, no. 9, p. 661, 2018.

[6] M. F. de Lange, K. J. Verouden, T. J. Vlugt, J. Gascon, and F. Kapteijn, "Adsorption-driven heat pumps: the potential of metal–organic frameworks," *Chemical Reviews*, vol. 115, no. 22, pp. 12205–12250, 2015.

[7] S. Chen, B. E. Lucier, P. D. Boyle, and Y. Huang, "Understanding the fascinating origins of co2 adsorption and dynamics in mofs," *Chemistry of Materials*, vol. 28, no. 16, pp. 5829–5846, 2016.

[8] H. Kim, S. R. Rao, E. A. Kapustin, L. Zhao, S. Yang, O. M. Yaghi, and E. N. Wang, "Adsorption-based atmospheric water harvesting device for arid climates," *Nature communications*, vol. 9, no. 1, pp. 1–8, 2018.

[9] M. J. Kalmutzki, C. S. Diercks, and O. M. Yaghi, "Metal–organic frameworks for water harvesting from air," *Advanced Materials*, vol. 30, no. 37, p. 1704304, 2018.

[10] M. Ejeian and R. Wang, "Adsorption-based atmospheric water harvesting," *Joule*, vol. 5, no. 7, pp. 1678–1703, 2021.

[11] S. Lee, B. Kim, H. Cho, H. Lee, S. Y. Lee, E. S. Cho, and J. Kim, "Computational screening of trillions of metal–organic frameworks for high-performance methane storage," *ACS Applied Materials & Interfaces*, 2021.

[12] A. Li, R. Bueno-Perez, S. Wiggin, and D. Fairen-Jimenez, "Enabling efficient exploration of metal–organic frameworks in the cambridge structural database," *CrystEngComm*, vol. 22, no. 43, pp. 7152–7161, 2020.

[13] R. Anderson, J. Rodgers, E. Argueta, A. Biong, and D. A. Gómez-Gualdrón, "Role of pore chemistry and topology in the co2 capture capabilities of mofs: from molecular simulation to machine learning," *Chemistry of Materials*, vol. 30, no. 18, pp. 6325–6337, 2018.

[14] P. Z. Moghadam, S. M. Rogge, A. Li, C.-M. Chow, J. Wieme, N. Moharrami, M. Aragones-Anglada, G. Conduit, D. A. Gomez-Gualdron, V. Van Speybroeck, *et al.*, "Structure-mechanical stability relations of metal-organic frameworks via machine learning," *Matter*, vol. 1, no. 1, pp. 219–234, 2019.

[15] M. Zhou, A. Vassallo, and J. Wu, "Toward the inverse design of mof membranes for efficient d2/h2 separation by combination of physics-based and data-driven modeling," *Journal of Membrane Science*, vol. 598, p. 117675, 2020.

[16] Y. Yan, Z. Shi, H. Li, L. Li, X. Yang, S. Li, H. Liang, and Z. Qiao, "Machine learning and in-silico screening of metal–organic frameworks for o2/n2 dynamic adsorption and separation," *Chemical Engineering Journal*, vol. 427, p. 131604, 2022.

[17] N. Rampal, A. Ajenifuja, A. Tao, C. Balzer, M. S. Cummings, A. Evans, R. Bueno-Perez, D. J. Law, L. W. Bolton, C. Petit, *et al.*, "The development of a comprehensive toolbox based on multi-level, high-throughput screening of mofs for co/n 2 separations," *Chemical Science*, vol. 12, no. 36, pp. 12068–12081, 2021.

[18] G. Avci, I. Erucar, and S. Keskin, "Do new mofs perform better for co2 capture and h2 purification? computational screening of the updated mof database," *ACS Applied Materials & Interfaces*, vol. 12, no. 37, pp. 41567–41579, 2020.

[19] P. Halder and J. K. Singh, "High-throughput screening of metal–organic frameworks for ethane–ethylene separation using the machine learning technique," *Energy & Fuels*, vol. 34, no. 11, pp. 14591–14597, 2020.

[20] W. Yang, H. Liang, F. Peng, Z. Liu, J. Liu, and Z. Qiao, "Computational screening of metal–organic framework membranes for the separation of 15 gas mixtures," *Nanomaterials*, vol. 9, no. 3, p. 467, 2019.

[21] Z. Qiao, L. Li, S. Li, H. Liang, J. Zhou, and R. Q. Snurr, "Molecular fingerprint and machine learning to accelerate design of high-performance homochiral metal–organic frameworks," *AIChE Journal*, vol. 67, no. 10, p. e17352, 2021.

[22] S. Li, Y. G. Chung, and R. Q. Snurr, "High-throughput screening of metal–organic frameworks for co2 capture in the presence of water," *Langmuir*, vol. 32, no. 40, pp. 10368–10376, 2016.

[23] M. Pardakhti, E. Moharreri, D. Wanik, S. L. Suib, and R. Srivastava, "Machine learning using combined structural and chemical descriptors for prediction of methane adsorption performance of metal organic frameworks (mofs)," *ACS combinatorial science*, vol. 19, no. 10, pp. 640–645, 2017.

[24] N. S. Bobbitt and R. Q. Snurr, "Molecular modelling and machine learning for high-throughput screening of metal-organic frameworks for hydrogen storage," *Molecular Simulation*, vol. 45, no. 14-15, pp. 1069–1081, 2019.

[25] Z. Qiao, Q. Xu, A. K. Cheetham, and J. Jiang, "High-throughput computational screening of metal–organic frameworks for thiol capture," *The Journal of Physical Chemistry C*, vol. 121, no. 40, pp. 22208–22215, 2017.

[26] H. Liang, W. Yang, F. Peng, Z. Liu, J. Liu, and Z. Qiao, "Combining large-scale screening and machine learning to predict the metal-organic frameworks for organosulfurs removal from high-sour natural gas," *APL Materials*, vol. 7, no. 9, p. 091101, 2019.

[27] P. Yang, G. Lu, Q. Yang, L. Liu, X. Lai, and D. Yu, "Analyzing acetylene adsorption of metal–organic frameworks based on machine learning," *Green Energy & Environment*, 2021.

[28] H. Dureckova, M. Krykunov, M. Z. Aghaji, and T. K. Woo, "Robust machine learning models for predicting high co2 working capacity and co2/h2 selectivity of gas adsorption in metal organic frameworks for precombustion carbon capture," *The Journal of Physical Chemistry C*, vol. 123, no. 7, pp. 4133–4139, 2019.

[29] Z. Liu, K. Zhang, Q. Xia, X. Wang, B. Huang, and H. Xi, "Predicting adsorption and separation performance indicators of xe/kr in metal-organic frameworks via a precursor-based neural network model," *Chemical Engineering Science*, vol. 243, p. 116772, 2021.

[30] P. Ma, J. Zhang, P. Liu, Q. Wang, Y. Zhang, K. Song, R. Li, and L. Shen, "Computer-assisted design for stable and porous metal-organic framework (mof) as a carrier for curcumin delivery," *LWT*, vol. 120, p. 108949, 2020.

[31] Z. Du, S. Deng, L. Zhao, Z. Ma, H. Bao, and J. Zhao, "A high-throughput computational screening of potential adsorbents for a thermal compression co 2 brayton cycle," *Sustainable Energy & Fuels*, vol. 5, no. 5, pp. 1415–1428, 2021.

[32] R. Long, X. Xia, Y. Zhao, S. Li, Z. Liu, and W. Liu, "Screening metal-organic frameworks for adsorption-driven osmotic heat engines via grand canonical monte carlo simulations and machine learning," *Iscience*, vol. 24, no. 1, p. 101914, 2021.

[33] Z. Shi, H. Liang, W. Yang, J. Liu, Z. Liu, and Z. Qiao, "Machine learning and in silico discovery of metal-organic frameworks: Methanol as a working fluid in adsorption-driven heat pumps and chillers," *Chemical Engineering Science*, vol. 214, p. 115430, 2020.

[34] Z. Shi, X. Yuan, Y. Yan, Y. Tang, J. Li, H. Liang, L. Tong, and Z. Qiao, "Techno-economic analysis of metal–organic frameworks for adsorption heat pumps/chillers: from directional computational screening, machine learning to experiment," *Journal of Materials Chemistry A*, vol. 9, no. 12, pp. 7656–7666, 2021.

[35] E. J. García, D. Bahamon, and L. F. Vega, "Systematic search of suitable metal–organic frameworks for thermal energy-storage applications with low global warming potential refrigerants," *ACS Sustainable Chemistry & Engineering*, vol. 9, no. 8, pp. 3157–3171, 2021.

[36] E. Brochu, V. M. Cora, and N. De Freitas, "A tutorial on bayesian optimization of expensive cost functions, with application to active user modeling and hierarchical reinforcement learning," *arXiv preprint arXiv:1012.2599*, 2010.

[37] M. Ahmadi, M. Vogt, P. Iyer, J. Bajorath, and H. Fröhlich, "Predicting potent compounds via model-based global optimization," *Journal of chemical information and modeling*, vol. 53, no. 3, pp. 553–559, 2013.

[38] B. Rohr, H. S. Stein, D. Guevarra, Y. Wang, J. A. Haber, M. Aykol, S. K. Suram, and J. M. Gregoire, "Benchmarking the acceleration of materials discovery by sequential learning," *Chemical Science*, vol. 11, no. 10, pp. 2696–2706, 2020.

[39] R. Aggarwal, M. Demkowicz, and Y. Marzouk, "Information-driven experimental design in materials science," in *Information science for materials discovery and design*, pp. 13–44, Springer, 2016.

[40] A. Seko, T. Maekawa, K. Tsuda, and I. Tanaka, "Machine learning with systematic density-functional theory calculations: Application to melting temperatures of single-and binary-component solids," *Physical Review B*, vol. 89, no. 5, p. 054303, 2014.

[41] S. Kiyohara, H. Oda, K. Tsuda, and T. Mizoguchi, "Acceleration of stable interface structure searching using a kriging approach," *Japanese Journal of Applied Physics*, vol. 55, no. 4, p. 045502, 2016.

[42] R. Dehghannasiri, D. Xue, P. V. Balachandran, M. R. Yousefi, L. A. Dalton, T. Lookman, and E. R. Dougherty, "Optimal experimental design for materials discovery," *Computational Materials Science*, vol. 129, pp. 311–322, 2017.

[43] P. G. Boyd, A. Chidambaram, E. García-Díez, C. P. Ireland, T. D. Daff, R. Bounds, A. Gładysiak, P. Schouwink, S. M. Moosavi, M. M. Maroto-Valer, *et al.*, "Data-driven design of metal–organic frameworks for wet flue gas co 2 capture," *Nature*, vol. 576, no. 7786, pp. 253–256, 2019.

[44] K. Choudhary, B. DeCost, and F. Tavazza, "Machine learning with force-field-inspired descriptors for materials: Fast screening and mapping energy landscape," *Physical review materials*, vol. 2, no. 8, p. 083801, 2018.

[45] A. Dunn, Q. Wang, A. Ganose, D. Dopp, and A. Jain, "Benchmarking materials property prediction methods: the matbench test set and automatminer reference algorithm," *npj Computational Materials*, vol. 6, no. 1, pp. 1–10, 2020.

[46] S. M. Lundberg and S.-I. Lee, "A unified approach to interpreting model predictions," in *Advances in Neural Information Processing Systems 30* (I. Guyon, U. V. Luxburg, S. Bengio, H. Wallach, R. Fergus, S. Vishwanathan, and R. Garnett, eds.), pp. 4765–4774, Curran Associates, Inc., 2017.

[47] J. Ling, M. Hutchinson, E. Antono, S. Paradiso, and B. Meredig, "High-dimensional materials and process optimization using data-driven experimental design with well-calibrated uncertainty estimates," *Integrating Materials and Manufacturing Innovation*, vol. 6, no. 3, pp. 207–217, 2017.

[48] S. N. Lophaven, H. B. Nielsen, J. Sondergaard, and A. Dace, "A matlab kriging toolbox," *Technical University of Denmark, Kongens Lyngby, Technical Report No. IMMTR-2002*, vol. 12, 2002.

[49] T. Ueno, T. D. Rhone, Z. Hou, T. Mizoguchi, and K. Tsuda, "Combo: an efficient bayesian optimization library for materials science," *Materials discovery*, vol. 4, pp. 18–21, 2016.

[50] M. Fasano, L. Bergamasco, A. Lombardo, M. Zanini, E. Chiavazzo, and P. Asinari, "Water/ethanol and 13x zeolite pairs for long-term thermal energy storage at ambient pressure," *Frontiers in Energy Research*, vol. 7, p. 148, 2019.

[51] M. Fasano, A. Bevilacqua, E. Chiavazzo, T. Humplik, and P. Asinari, "Mechanistic correlation between water infiltration and framework hydrophilicity in mfi zeolites," *Scientific reports*, vol. 9, no. 1, pp. 1–12, 2019.

[52] M. Neri, E. Chiavazzo, and L. Mongibello, "Numerical simulation and validation of commercial hot water tanks integrated with phase change material-based storage units," *Journal of Energy Storage*, vol. 32, p. 101938, 2020.

[53] L. Ward, A. Dunn, A. Faghaninia, N. E. Zimmermann, S. Bajaj, Q. Wang, J. Montoya, J. Chen, K. Bystrom, M. Dylla, *et al.*, "Matminer: An open source toolkit for materials data mining," *Computational Materials Science*, vol. 152, pp. 60–69, 2018.

[54] M. Fasano, D. Borri, E. Chiavazzo, and P. Asinari, "Protocols for atomistic modeling of water uptake into zeolite crystals for thermal storage and other applications," *Applied Thermal Engineering*, vol. 101, pp. 762–769, 2016.

[55] M. Fasano, G. Falciani, V. Brancato, V. Palomba, P. Asinari, E. Chiavazzo, and A. Frazzica, "Atomistic modelling of water transport and adsorption mechanisms in silicoaluminophosphate for thermal energy storage," *Applied Thermal Engineering*, vol. 160, p. 114075, 2019.

[56] X. Wu, S. Xiang, J. Su, and W. Cai, "Understanding quantitative relationship between methane storage capacities and characteristic properties of metal–organic frameworks based on machine learning," *The Journal of Physical Chemistry C*, vol. 123, no. 14, pp. 8550–8559, 2019.

[57] X. Yu, S. Choi, D. Tang, A. J. Medford, and D. S. Sholl, "Efficient models for predicting temperature-dependent henry's constants and adsorption selectivities for diverse collections of molecules in metal–organic frameworks," *The Journal of Physical Chemistry C*, vol. 125, no. 32, pp. 18046–18057, 2021.

[58] L. Lavagna, D. Burlon, R. Nisticò, V. Brancato, A. Frazzica, M. Pavese, and E. Chiavazzo, "Cementitious composite materials for thermal energy storage applications: a preliminary characterization and theoretical analysis," *Scientific Reports*, vol. 10, no. 1, pp. 1–13, 2020.

[59] L. Talirz, S. Kumbhar, E. Passaro, A. V. Yakutovich, V. Granata, F. Gargiulo, M. Borelli, M. Uhrin, S. P. Huber, S. Zoupanos, *et al.*, "Materials cloud, a platform for open computational science," *Scientific data*, vol. 7, no. 1, pp. 1–12, 2020.

[60] H.-J. Butt, K. Graf, and M. Kappl, *Physics and chemistry of interfaces*. John Wiley & Sons, 2013.

[61] D. M. Ruthven, *Principles of adsorption and adsorption processes*. John Wiley & Sons, 1984.

[62] F. P. Schmidt, *Optimizing Adsorbents for Heat Storage Applications: Estimation of Thermodynamic Limits and Monte Carlo Simulations of Water Adsorption in Nanopores*. PhD thesis, 2004.

[63] K. S. Sing, "Reporting physisorption data for gas/solid systems with special reference to the determination of surface area and porosity (recommendations 1984)," *Pure and applied chemistry*, vol. 57, no. 4, pp. 603–619, 1985.

[64] J. A. Dean, "Lange's handbook of chemistry," *Material and manufacturing process*, vol. 5, no. 4, pp. 687–688, 1990.

[65] I. Dincer and M. A. Rosen, *Thermal energy storage systems and applications*. John Wiley & Sons, 2021.

[66] L. M. Ghiringhelli, J. Vybiral, S. V. Levchenko, C. Draxl, and M. Scheffler, "Big data of materials science: critical role of the descriptor," *Physical review letters*, vol. 114, no. 10, p. 105503, 2015.

[67] S. I. Gomes, M. J. Amorim, S. Pokhrel, L. Mädler, M. Fasano, E. Chiavazzo, P. Asinari, J. Jänes, K. Tämm, J. Burk, *et al.*, "Machine learning and materials modelling interpretation of in vivo toxicological response to tio 2 nanoparticles library (uv and non-uv exposure)," *Nanoscale*, vol. 13, no. 35, pp. 14666–14678, 2021.

[68] E. Chiavazzo, R. Covino, R. R. Coifman, C. W. Gear, A. S. Georgiou, G. Hummer, and I. G. Kevrekidis, "Intrinsic map dynamics exploration for uncharted effective free-energy landscapes," *Proceedings of the National Academy of Sciences*, vol. 114, no. 28, pp. E5494–E5503, 2017.

Acknowledgments

E.C. acknowledges financial support of the Italian National Project PRIN *Heat transfer and Thermal Energy Storage Enhancement by Foams and Nanoparticles* (2017F7KZWS) and of the research contract PTR 2019/21 ENEA (*Sviluppo di modelli per la caratterizzazione delle proprietà di scambio termico di PCM in presenza di additivi per il miglioramento dello scambio termico*) funded by the Italian Ministry of Economic Development (MiSE).

Authors contributions

E.C. conceived the idea and found financial support. G.T. performed all computations and wrote the first paper draft. E.C., M.F and L.B. supervised the research activities. L.B. and M.F. helped with result presentation and interpretation. M.F. suggested the synthetic dataset. All authors contributed to final paper writing.

Competing interests

The authors declare no competing interests.

arXiv:2111.09602v1 [cond-mat.other] 18 Nov 2021

Supplementary Information for:

Minimal set of crystallographic descriptors for sorption properties in hypothetical Metal Organic Frameworks: Role in sequential learning optimization

Giovanni Trezza, Luca Bergamasco, Matteo Fasano, Eliodoro Chiavazzo*

Department of Energy, Politecnico di Torino, C.so Duca degli Abruzzi 24, Torino 10129, Italy

S1: Synthetic dataset

We have generated a synthetic dataset of 1000 samples and 20 columns by means of the "Friedman #1" regression problem [8, 2, 1], in which the target y is given by the combination of five independent variables ($\mathbf{x} \in \mathbb{R}^5$):

$$y(\mathbf{x}) = 10\sin(\pi x_1 x_2) + 20\left(x_3 - \frac{1}{2}\right)^2 + 10x_4 + 5x_5 + \epsilon\mathcal{N}(0,1) \tag{1}$$

choosing a zero-centered and unit-variance noisy term normally distributed $\mathcal{N}(0,1)$, with $\epsilon = 0.1$. More specifically, all the descriptors are independent and uniformly distributed over the interval $[0,1]$, but only 5 of them are effectively used to compute the output. Therefore, the remaining 15 columns represent *fake* features, with the only purpose of disturbing the regression model.

For the identification of the important features, we have applied the model-agnostic interpretability algorithm of Kernel SHAP on a working regression model constructed with AutoMatminer. In particular, AutoMatminer trained a model on the 80% of the 1000 samples by means of the "express" preset and tested it over the remaining 20%, getting a regression performance of $R^2 = 0.978$ (Fig. S1). Afterwards, we have computed the impact of each input to the model output by means of the Kernel SHAP algorithm, which is able to recognize the five important features among the twenty defined beforehand; indeed, the descriptors $(x_6, \ldots, x_{20})$ have negligible coefficients of importance with respect to the $(x_1, \ldots, x_5)$ ones (Fig. S2).

We have checked the performance of all the regression methodologies (RF-Random Forest, K-Kriging, COMBO) with the related acquisition functions (MEI, MLI, MU, PI, EI) over both the whole synthetic dataset (20 features) and its reduced version (the 5 most important features). In particular, we aimed at finding the maximum among a random subset of 300 samples from the original 1000 rows long dataset, starting with the pool of 30 points with the lowest target y. We note that, in general, having a smaller number of descriptors (albeit the meaningful ones) does not allow a faster convergence; anyway, having a feature space with lower dimension implies a lower computational burden of the SL procedure. Figure S3 shows the main results.

*Corresponding author: eliodoro.chiavazzo@polito.it

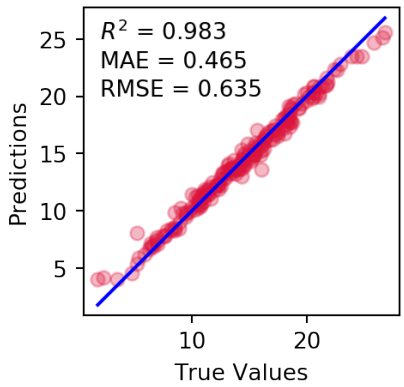


Figure S1: Predictions of the regression model trained with AutoMatminer (preset "express" of the "Friedman#1" problem) over the testing set. Model performance measures are shown in terms of coefficient of determination R^2, Mean Absolute Error (MAE), Root Mean Squared Error (RMSE).

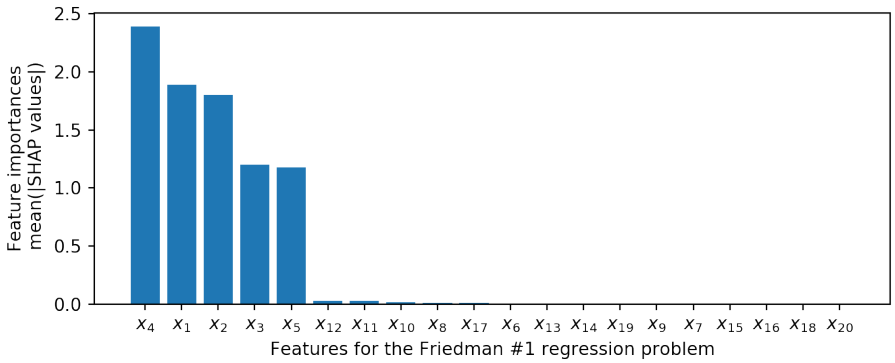


Figure S2: Average impact of the 20 features on the model output for the "Friedman#1" regression problem over the whole testing set (200 samples) by Kernel SHAP, which recognizes correctly that only features $(x_1, \ldots, x_5)$ are relevant.

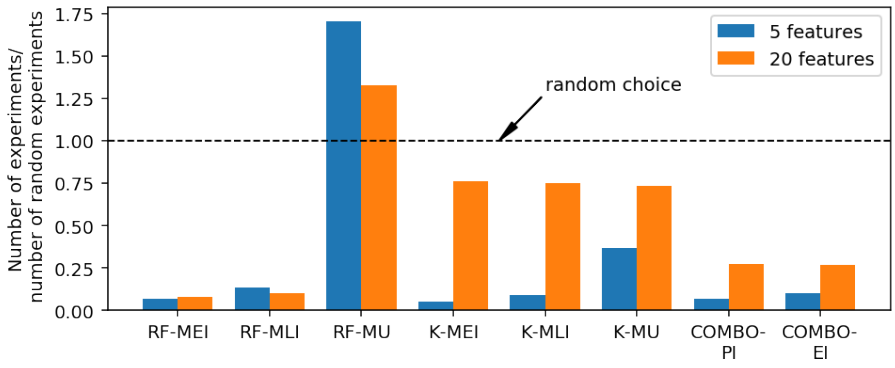


Figure S3: Number of evaluations before the convergence to the maximum in the synthetic example for the SL algorithms normalized with respect to the random choice (corresponding to 135 experiments). The initial set consists of the same worst 30 candidates (in terms of the target property) from a random subset of 300 samples of the original dataset.

S2: Lists of the retained variables

Table S1: List of the 44 features retained by AutoMatminer to train the regression model of the Henry coefficient for CO_2. The reported order is dictated by the SHAP analysis, in accordance with the reported cumulative importance percentage.

Descriptors AutoMatminer	Cumulative importance percentage (%)	Descriptors AutoMatminer	Cumulative importance percentage (%)
'jml_log_vpa'	19.01	'jml_nn_72'	1.87
'jml_nn_75'	5.56	'jml_rdf_54'	1.80
'jml_first_ion_en_mult_voro_coord'	5.24	'jml_X_mult_voro_coord'	1.59
'jml_rdf_22'	4.35	'jml_rdf_48'	1.43
'jml_C-14'	3.45	'jml_nn_85'	1.32
'jml_nn_15'	3.23	'jml_nn_38'	1.16
'jml_nn_87'	3.15	'jml_rdf_61'	1.07
'jml_X_add_voro_coord'	2.96	'jml_rdf_34'	1.05
'jml_rdf_23'	2.90	'jml_rdf_38'	1.01
'jml_nn_25'	2.83	'jml_mean_charge_13'	1.00
'jml_nn_78'	2.70	'jml_rdf_35'	0.92
'jml_rdf_76'	2.61	'jml_nn_80'	0.83
'jml_nn_77'	2.49	'jml_nn_71'	0.78
'jml_nn_84'	2.35	'jml_rdf_60'	0.76
'jml_nn_79'	2.33	'jml_nn_65'	0.53
'jml_nn_86'	2.18	'jml_rdf_21'	0.52
'jml_nn_74'	2.09	'jml_pack_frac'	0.50
'jml_nn_82'	2.07	'jml_nn_21'	0.42
'jml_rdf_80'	2.06	'jml_rdf_28'	0.34
'jml_rdf_73'	2.03	'jml_nn_50'	0.32
'jml_nn_81'	1.89	'jml_nn_73'	0.31
'jml_nn_76'	1.88	'jml_rdf_79'	0.00

Table S2: List of the 92 features retained by AutoMatminer to train the regression model of the working capacity for CO_2. The reported order is dictated by the SHAP analysis, in accordance with the reported cumulative importance percentage.

Descriptors AutoMatminer	Cumulative importance percentage (%)	Descriptors AutoMatminer	Cumulative importance percentage (%)
'jml_vpa'	6.80	'jml_nn_76'	0.85
'jml_nn_11'	4.74	'jml_rdf_35'	0.82
'jml_nn_25'	4.47	'jml_rdf_48'	0.80
'jml_rdf_10'	3.91	'jml_nn_79'	0.79
'jml_rdf_14'	2.49	'jml_rdf_64'	0.78
'jml_rdf_54'	2.47	'jml_rdf_67'	0.78
'jml_rdf_53'	2.36	'jml_nn_75'	0.76
'jml_nn_22'	2.13	'jml_rdf_40'	0.75
'jml_atom_mass_divi_bp'	2.09	'jml_nn_89'	0.74
'jml_nn_55'	2.07	'jml_nn_34'	0.72
'jml_rdf_52'	2.04	'jml_nn_30'	0.67
'jml_rdf_51'	1.80	'jml_nn_70'	0.65
'jml_rdf_56'	1.74	'jml_nn_80'	0.65
'jml_rdf_21'	1.66	'jml_nn_77'	0.61
'jml_nn_38'	1.57	'jml_rdf_39'	0.54
'jml_rdf_24'	1.49	'jml_nn_15'	0.52
'jml_elec_aff_mult_voro_coord'	1.49	'jml_rdf_71'	0.52
'jml_rdf_58'	1.44	'jml_hfus_add_X'	0.47
'jml_rdf_15'	1.37	'jml_rdf_77'	0.45
'jml_nn_87'	1.36	'jml_rdf_76'	0.43
'jml_rdf_31'	1.35	'jml_rdf_87'	0.40
'jml_nn_54'	1.35	'jml_elec_aff_add_X'	0.38
'jml_rdf_37'	1.34	'jml_rdf_34'	0.38
'jml_rdf_55'	1.28	'jml_nn_32'	0.37
'jml_nn_40'	1.24	'jml_nn_73'	0.37
'jml_rdf_60'	1.23	'jml_rdf_36'	0.37
'jml_rdf_59'	1.21	'jml_rdf_86'	0.36
'jml_elec_aff_mult_atom_mass'	1.20	'jml_rdf_73'	0.36
'jml_nn_27'	1.18	'jml_nn_69'	0.34
'jml_nn_78'	1.15	'jml_nn_20'	0.33
'jml_nn_33'	1.11	'jml_nn_66'	0.32
'jml_rdf_57'	1.04	'jml_nn_50'	0.31
'jml_rdf_13'	0.94	'jml_mol_vol_divi_atom_rad'	0.31
'jml_rdf_69'	0.94	'jml_nn_71'	0.30
'jml_nn_46'	0.94	'jml_adf1_52'	0.30
'jml_rdf_50'	0.93	'jml_rdf_44'	0.25
'jml_rdf_88'	0.93	'jml_rdf_80'	0.25
'jml_rdf_61'	0.92	'jml_adf1_1'	0.25
'jml_nn_53'	0.91	'jml_nn_72'	0.24
'jml_rdf_75'	0.91	'jml_nn_24'	0.00
'jml_nn_29'	0.90	'jml_rdf_26'	0.00
'jml_nn_39'	0.89	'jml_nn_14'	0.00
'jml_nn_96'	0.89	'jml_rdf_22'	0.00
'jml_nn_92'	0.88	'jml_rdf_23'	0.00
'jml_rdf_78'	0.87	'jml_rdf_70'	0.00
'jml_nn_21'	0.86	'jml_nn_16'	0.00

Table S3: List of the 36 features retained by AutoMatminer to train the regression model of the Henry coefficient for H_2O. The reported order is dictated by the SHAP analysis, in accordance with the reported cumulative importance percentage.

Descriptors AutoMatminer	Cumulative importance percentage (%)	Descriptors AutoMatminer	Cumulative importance percentage (%)
'jml_C-14'	36.14	'jml_nn_25'	1.21
'jml_rdf_22'	5.41	'jml_rdf_26'	1.89
'jml_rdf_38'	5.16	'jml_jv_enp'	1.15
'jml_nn_10'	4.92	'jml_nn_79'	1.10
'jml_nn_22'	4.77	'jml_polzbl_add_first_ion_en'	1.04
'jml_X_add_voro_coord'	3.58	'jml_nn_14'	0.93
'jml_log_vpa'	3.40	'jml_mol_vol_divi_atom_rad'	0.89
'jml_nn_13'	3.06	'jml_adf1_175'	0.83
'jml_nn_23'	2.85	'jml_nn_11'	0.58
'jml_bp_mult_atom_mass'	2.84	'jml_rdf_75'	0.53
'jml_nn_20'	2.63	'jml_nn_81'	0.50
'jml_nn_15'	2.52	'jml_nn_44'	0.48
'jml_nn_17'	2.20	'jml_nn_21'	0.42
'jml_nn_16'	1.86	'jml_rdf_21'	0.30
'jml_rdf_36'	1.82	'jml_rdf_66'	0.29
'jml_rdf_16'	1.68	'jml_nn_65'	0.13
'jml_nn_38'	1.46	'jml_bp_divi_hfus'	0.00
'jml_hfus_add_X'	1.30	'jml_rdf_80'	0.00

Table S4: List of the 24 features retained by AutoMatminer to train the regression model of the surface area. The reported order is dictated by the SHAP analysis, in accordance with the reported cumulative importance percentage.

Descriptors AutoMatminer	Cumulative importance percentage (%)	Descriptors AutoMatminer	Cumulative importance percentage (%)	Descriptors AutoMatminer	Cumulative importance percentage (%)
'jml_vpa'	46.80	'jml_nn_78'	2.26	'jml_nn_73'	1.43
'jml_pack_frac'	11.39	'jml_rdf_48'	2.20	'jml_rdf_53'	1.09
'jml_nn_75'	4.03	'jml_nn_80'	2.17	'jml_rdf_73'	0.84
'jml_nn_81'	3.95	'jml_nn_74'	1.81	'jml_rdf_45'	0.83
'jml_nn_82'	3.59	'jml_nn_54'	1.77	'jml_nn_45'	0.77
'jml_nn_55'	2.79	'jml_nn_72'	1.69	'jml_rdf_55'	0.75
'jml_nn_67'	2.54	'jml_nn_57'	1.69	'jml_rdf_60'	0.59
'jml_nn_77'	2.31	'jml_nn_71'	1.54	'jml_rdf_57'	0.00

S3: List of the retained AutoMatminer operators

Table S5: List of the retained AutoMatminer operators. The non tpot.X-type operators are intended to be sklearn operators.

Feature preprocessors	Feature selectors
preprocessing.Binarizer	feature_selection.SelectPercentile
decomposition.FastICA	
cluster.FeatureAgglomeration	
preprocessing.MaxAbsScaler	
preprocessing.MinMaxScaler	
kernel_approximation.Nystroem	
decomposition.PCA	
preprocessing.PolynomialFeatures	
kernel_approximation.RBFSampler	
preprocessing.RobustScaler	
preprocessing.StandardScaler	
tpot.builtins.ZeroCount	
tpot.builtins.OneHotEncoder	
ML-models	
ensemble.ExtraTreesRegressor	
ensemble.GradientBoostingRegressor	
tree.DecisionTreeRegressor	
neighbors.KNeighborsRegressor	
ensemble.RandomForestRegressor	
linear_model.RidgeCV	

S4: Determination of the proportionality constant between water uptake and surface area

H_2O working capacity is necessary to convert the Henry coefficient to units of Pa^{-1}, but no data are available from the database we referred to. Therefore we rely on MOFs specific surface area instead. In detail, Chaemchuen *et al.* have reported H_2O working capacity for a pool of 66 MOFs [5]. As shown in Fig. S4, a good correlation between the water uptake and the surface area (i.e., the available internal surface per gram of dry adsorbent) can be observed with a Pearson coefficient of $\rho = 0.817$, where we have assumed density of H_2O being $1\,g_{H_2O}/cm^3_{H_2O}$. On the basis of that correlation, linear regression is imposed for finding the constant of proportionality for the pair water uptake vs the surface area (water uptake $= \eta \times$ surface area). This yields $\eta = 3.875 \times 10^{-4}\,g_{H_2O}/m^2$.

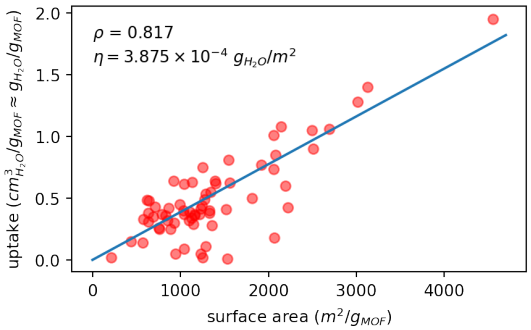


Figure S4: Water uptake against surface area for 66 potential MOFs from the database by Chaemchuen *et al.* [5]. The Pearson coefficient ρ between those two quantities is shown. The linear regression (blue line) gives a constant of proportionality η, such that uptake $= \eta \times$ surface area, in the approximation that $1\,g_{H_2O}$ occupies a volume of $1\,cm^3_{H_2O}$.

S5: Determination of isotherms at different temperatures based on the Polanyi theory

In the MOFs database we referred to, the Henry coefficient for H_2O is given only at $T = 298\,\mathrm{K}$, while we needed isotherms at $T_A = 308\,\mathrm{K}$ and $T_C = 353\,\mathrm{K}$. To overcome this issue, we have used the Polanyi theory for rescaling the FFG modeled curve at different temperatures.

We have checked the validity of this method by means of three experimental isotherms at 298 K, 313 K, 333 K for the water adsorption on MOF Al-fumarate [11]. In particular, we have made a regression over the experimental curve at 298 K employing the FFG model with $\beta = 3.9$ and $H(T = 298\,\mathrm{K}) = 1.4 \times 10^{-4}\,\mathrm{Pa}^{-1}$ (Fig. S6, above left). Then, we have rescaled the abscissa of this fitted curve using the Polanyi procedure. Fig. S5 shows general agreement between the experimental isotherms and the corresponding rescaled ones at 313 K and 333 K.

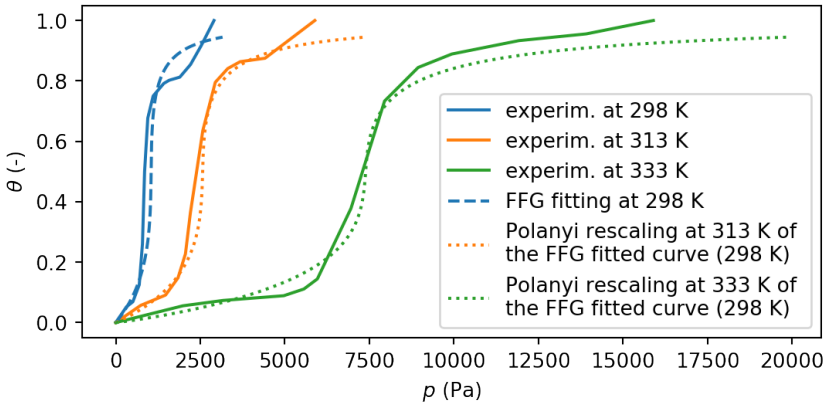


Figure S5: Solid curve: experimental isotherms for water on MOF Al-fumarate at 298 K (blue), 313 K (orange), 333 K (green). Dashed blue curve: FFG fitting of the experimental isotherm at 298 K ($H(T = 298\,\mathrm{K}) = 1.4 \times 10^{-4}\,\mathrm{Pa}^{-1}$, $\beta = 3.9$). Dotted curves: rescaling of the FFG modeled isotherm (blue dashed curve) at 313 K (orange) and 333 K (green) according to the Polanyi theory.

S6: Determination of the average β for the FFG model

For all the potential MOFs, we have used the average value $\beta = 3.4$ in the identification of the isotherm curves according to the FFG model (Eq. 2). For achieving this, we have considered 8 real MOF-water pairs where the isotherm curve (at 298 K or 293 K) is known in the chart "uptake" against "relative pressure $p/p_s(T)$". We have considered the last experimental point to be at $\theta = 1$, and rescaled the horizontal axis by $p_s(T)$ (Antoine equation), obtaining the usual $\theta - p$ chart. Hence, we have determined, for each of the compounds, the Henry coefficient in units of Pa^{-1}, by exploiting the low pressure approximation $\theta = H(T)p$. Finally, we have identified for all the MOFs 25 isotherms following the FFG model, with $\beta = 1.5, 1.6, \ldots, 3.9$. The best value of β has been determined as the one optimizing a least squares problem with respect to the real isotherm. Results are reported in Fig. S6.

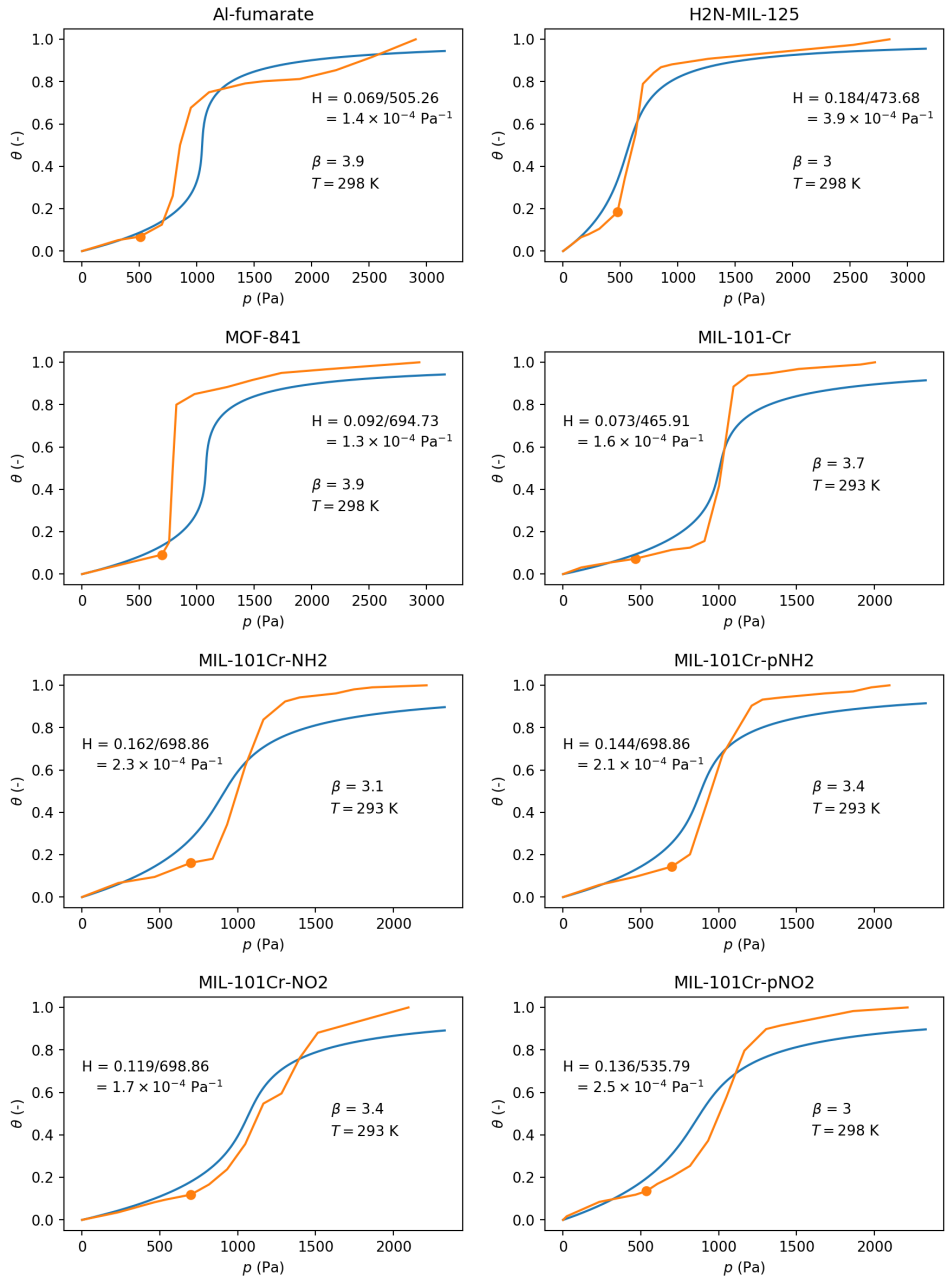


Figure S6: Fitting (blue curves) of the experimental isotherms (orange curves) for 8 MOF-water pairs: Al-fumarate [11], H_2N-MIL-125 [12], MOF-841 [9], MIL-101-Cr, MIL-101Cr-NH_2, MIL-101Cr-pNH_2, MIL-101Cr-NO_2, MIL-101Cr-pNO_2 [13]. For each MOF, the orange marker represents the point at which the H_2O Henry coefficient has been measured as θ/p. The best value of β is shown, with the temperature related to the curve.

S7: Regression methodologies for SL

Random forest regression. In general, a random forest approach [3] produces a number of decision trees, consisting in random partitions of the input space. On each one of them, a function (i.e., a decision tree) with a low generalization power is built, and their predictions are finally aggregated by taking the mean). The uncertainty of a prediction is a measure of its robustness, i.e., of how much every single known point of the training set influences the predicted value. Here, the Random Forest regression is implemented by means of the Lolo Scala library [10] and does not allow deterministic predictions (i.e., different runs with the same training set give, in general, different responses).

In particular, Ling *et al.* [10], following the approach by Efron [7] and Wager *et al.* [21], define the uncertainty as

$$\sigma(\mathbf{x}) = \sqrt{\left(\sum_{i=1}^{n} \max[\sigma_i^2(\mathbf{x}), \omega]\right) + \widetilde{\sigma}^2(\mathbf{x})} \tag{2}$$

where $\sigma_i^2(\mathbf{x})$ is the variance at the generic test-point $\mathbf{x}$ due to the i-th training point, $\omega = |\min_i \sigma^2(\mathbf{x}_i)|$ is a noise threshold and $\widetilde{\sigma}^2(\mathbf{x})$ is an explicit bias function. Specifically:

$$\sigma_i^2(\mathbf{x}) = \mathrm{Cov}_j[n_{i,j}, t_j(\mathbf{x})]^2 + [\bar{t}_{-i}(\mathbf{x}) - \bar{t}(\mathbf{x})]^2 - \frac{ev}{\mathcal{T}}, \tag{3}$$

where Cov_j is the covariance over the j-th tree, $n_{i,j}$ the number of instances of the i-th training point used to fit the j-th tree with prediction $t_j(\mathbf{x})$, $\bar{t}_{-i}(\mathbf{x})$ and $\bar{t}(\mathbf{x})$ are the average over trees not trained on sample i and the average over all the trees respectively, e is the Euler's number, v the variance over all the trees, $\mathcal{T}$ the number of trees. Figure S7 shows a scheme of a random forest regression.

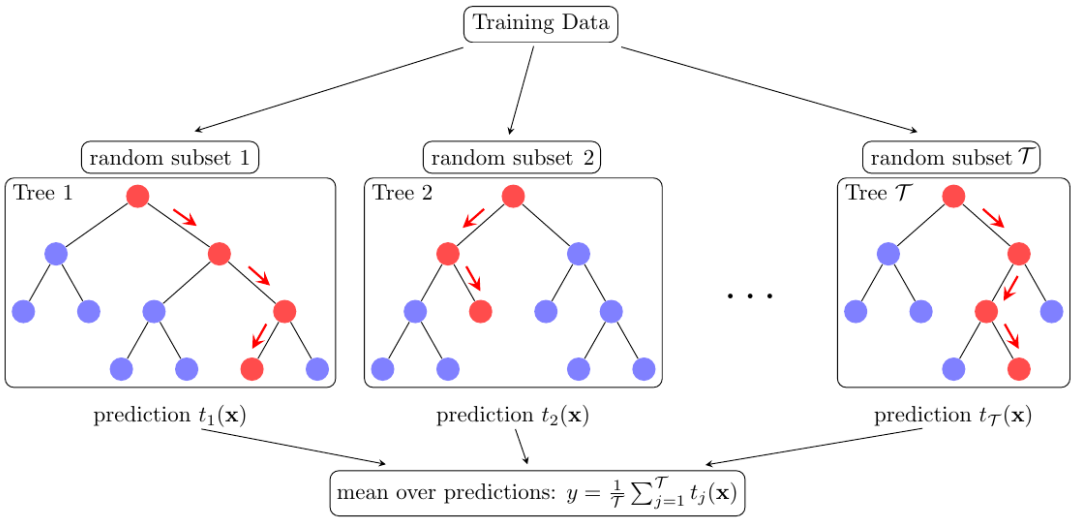


Figure S7: Random Forest scheme. Different random subsets of the training data are used to train different decision trees, each one with a low predictive power. Those predictions are aggregated by taking the mean.

Kriging. The kriging algorithm, which finds in geostatistics its original field of application [6], in the Matlab DACE package implementation [17] allows deterministic predictions (i.e., different runs with the same training set give the same response). The estimated value of the function is the result of a least squares approach; the uncertainty is the square root of the Mean Squared Error $\sqrt{MSE}$ (as meant by Lophaven *et al.* [17]), and depends on the correlation between the stochastic processes modeling the deviations from the predicted value.

In particular, a regression model $\mathcal{F}(\boldsymbol{\beta}, \mathbf{x})$ is given as a linear combination of r chosen functions

$$\mathcal{F}(\boldsymbol{\beta}, \mathbf{x}) = \mathbf{g}(\mathbf{x})^T \boldsymbol{\beta} = \beta_1 g_1(\mathbf{x}) + \cdots + \beta_r g_r(\mathbf{x}) \tag{4}$$

where $\boldsymbol{\beta}$ is the array of regression parameters; a suitable stochastic process $z(\cdot)$ is also defined in such a way that, given two domain points $\mathbf{x}, \mathbf{w} \in \mathbb{R}^d$, the following holds:

$$\mathbb{E}[z(\mathbf{x})z(\mathbf{w})] \propto \mathcal{R}(\boldsymbol{\gamma}, \mathbf{x}, \mathbf{w}), \tag{5}$$

where $\mathbb{E}[\cdot]$ denotes the expected value, $\boldsymbol{\gamma}$ is the array of parameters governing the correlation model $\mathcal{R}(\boldsymbol{\gamma}, \mathbf{x}, \mathbf{w})$; for the typical Gaussian shape (used here), it takes the form $\mathcal{R}(\boldsymbol{\gamma}, \mathbf{x}, \mathbf{w}) = \prod_{j=1}^{d} \exp(\gamma_j (w_j - x_j)^2)$.

For the set of the known $\mathbf{x}_1, \ldots, \mathbf{x}_n$, we consider the matrix $\mathbf{G} = [\mathbf{g}(\mathbf{x}_1), \ldots, \mathbf{g}(\mathbf{x}_n)]^T$, with $\mathbf{g}(\mathbf{x})$ defined in Eq. 4. Given the array of known responses $\mathbf{y} = [y_1, \cdots, y_n]^T$ and the corresponding errors $\mathbf{Z} = [z_1, \cdots, z_n]^T$, the mean value at the generic point $\mathbf{x}$ is computed by means of the linear predictor $\mu(\mathbf{x}) = \mathbf{c}^T \mathbf{y}$, where $\mathbf{c} \in \mathbb{R}^n$ comes from the minimization of the error $\mu(\mathbf{x}) - y(\mathbf{x}) = \mathbf{c}^T \mathbf{Z} - z(\mathbf{x}) + (\mathbf{G}^T \mathbf{c} - \mathbf{g}(\mathbf{x}))^T \boldsymbol{\beta}$. The mean squared error (MSE) for the unbiased predictor is strightforwardly $\sigma^2(\mathbf{x}) = \mathbb{E}[(\mu(\mathbf{x}) - y(\mathbf{x}))^2] = \mathbb{E}[(\mathbf{c}^T \mathbf{Z} - z(\mathbf{x}))^2]$.

Here, we have chosen a constant regression model $\mathcal{F}(\boldsymbol{\beta}, \mathbf{x})$, with $r = 1$, $g_1(\mathbf{x}) = 1$, the initial guess of the correlation parameter $\boldsymbol{\gamma} = \{1\}_d$, with bounds of 10^{-5} and 2.

Gaussian Process Regression. Gaussian Processes (GPs) construct a multivariate Gaussian distribution for any point to be evaluated; in this COMmon Bayesian Optimization Library (COMBO, `https://github.com/tsudalab/combo3`) implementation is not deterministic.

In particular, for the array of the function values $(\mathbf{y}, y_{n+1})^T \in \mathbb{R}^{n+1}$, $\mathbf{y} \in \mathbb{R}^n$ are the known responses, while $y_{n+1} \in \mathbb{R}$ is unknown. A kernel (covariance) matrix is constructed with entries K_{ij} depending on the distances between the arguments $||\mathbf{x}_i - \mathbf{x}_j||$ for the values $y_1, \ldots, y_{n+1}$. It gives rise to the zero-centered multivariate normal distribution

$$\begin{pmatrix} \mathbf{y} \\ y_{n+1} \end{pmatrix} \sim \mathcal{N}\left(\mathbf{0}, \begin{pmatrix} \mathbf{K} + \sigma_y^2 \mathbf{I} & \mathbf{k} \\ \mathbf{k}^T & k \end{pmatrix}\right) \tag{6}$$

where, given the zero-centered Gaussian distributed noise $\epsilon \sim \mathcal{N}(0, \sigma_y^2)$ on the perturbed function $y = f(\mathbf{x}) + \epsilon$ and the identity matrix $\mathbf{I}$, the predicted value is $\mu(\mathbf{x}_{n+1}) = \mathbb{E}[y_{n+1}] = \mathbf{k}^T (\mathbf{K} + \sigma_y^2 \mathbf{I})^{-1} \mathbf{y}$ with a related variance $\sigma^2(\mathbf{x}_{n+1}) = k - \mathbf{k}^T (\mathbf{K} + \sigma_y^2 \mathbf{I})^{-1} \mathbf{k}$ [19].

Here we have used the default squared exponential kernel provided by the COMBO library, by which $K_{ij} = \sigma_0^2 \exp(||\mathbf{x}_i - \mathbf{x}_j||^2 \ell^{-2}/2)$, where σ_0 (scale factor) and ℓ (width factor) are hyperparameters tuned automatically by means of an embedded stochastic-based ADAM optimization algorithm [20, 14]. COMBO, indeed, does not allow deterministic predictions.

S8: Query strategies

S8.1 Strategies for Random Forest and Kriging

Ling *et al.* [16], through different combinations of the predicted value $\mu(\mathbf{x}_i)$ and variance $\sigma(\mathbf{x}_i)$, propose three strategies for selecting the next candidate to test: *Maximum Expected Improvement* (MEI), *Maximum Uncertainty* (MU) and *Maximum Likelihood Improvement* (MLI).

- MEI strategy chooses the candidate with the maximum predicted value, i.e.,

$$\mathbf{x}_{MEI} = \arg \max_{i=n+1,\dots,m} \mu(\mathbf{x}_i). \tag{7}$$

- MU strategy chooses the candidate with the maximum uncertainty, i.e.,

$$\mathbf{x}_{MU} = \arg \max_{i=n+1,\dots,m} \sigma(\mathbf{x}_i). \tag{8}$$

- MLI strategy chooses the candidate that the most likely has a higher value than the best previously tested point, i.e.,

$$\mathbf{x}_{MLI} = \arg \max_{i=n+1,\dots,m} -\frac{|\mu(\mathbf{x}_i) - \max_{j=1,\dots,n} y_j|}{\sigma(\mathbf{x}_i)}. \tag{9}$$

Since variances tend to be high in poorly explored regions, MEI implements a purely *exploitative* strategy, while MU a purely *explorative* strategy. In this context, MLI represents a trade-off between the two needs: it takes into account high-performing candidates (exploitation) with sufficient uncertainty (exploration) to have a high likelihood of getting a better test-point. In this work, we have used the same query strategies for the kriging regression too.

S8.2 Strategies for Gaussian Processes

We have taken into account two of the possible acquisition functions provided by the COMBO library, i.e., Probability of Improvement (PI) and Expected Improvement (EI).

- Kushner [15] defines the Probability of Improvement as a criterion for maximizing the quantity

$$PI(\mathbf{x}) = P\left(f(\mathbf{x}) \geq \max_{i=1,\dots,n} y_i - \xi\right) = \Phi(Z) \tag{10}$$

  where $Z = \left(\mu(\mathbf{x}) - \max_{i=1,\dots,n} y_i\right)/\sigma(\mathbf{x})$, $\Phi(\cdot)$ denotes the CDF of a normal distribution and ξ is a trade-off parameter, whose choice is left to the user. Therefore, according to the PI strategy, the next point to query fulfils

$$\mathbf{x}_{PI} = \arg \max_{i=n+1,\dots,m} PI(\mathbf{x}_i). \tag{11}$$

  Since we have chosen $\xi = 0$, this strategy is purely exploitative.

- Močkus *et al.* [18] define the Improvement as $I(\mathbf{x}) = \max\{0, f(\{\mathbf{x}\}_{n+1}^m) - \max_{i=1,\dots,n} y_i\}$, which is positive when the next query point is greater than the best tested point so far. Its expected value turns out to be

$$\mathbb{E}[I(\mathbf{x})] = \begin{cases} \left(\mu(\mathbf{x}) - \max_{i=1,\dots,n} y_i\right)\Phi(Z) + \sigma(\mathbf{x})\phi(Z) & \text{if } \sigma(\mathbf{x}) > 0 \\ 0 & \text{if } \sigma(\mathbf{x}) = 0 \end{cases} \tag{12}$$

where $Z = (\mu(\mathbf{x}) - \max_{i=1,\dots,n} y_i)/\sigma(\mathbf{x})$, while $\phi(\cdot)$ and $\Phi(\cdot)$ denote respectively the PDF and the CDF of a normal distribution. Hence, according to the EI strategy, the next point to query fulfils

$$\mathbf{x}_{EI} = \arg \max_{i=n+1,\dots,m} \mathbb{E}[I(\mathbf{x}_i)], \tag{13}$$

which takes into account both the probability of improvement and the potential magnitude of the improvement a point can provide [4].

References

[1] sklearn.datasets.make_friedman1. `https://scikit-learn.org/stable/modules/generated/sklearn.datasets.make_friedman1.html`.

[2] Leo Breiman. Bagging predictors. *Machine learning*, 24(2):123–140, 1996.

[3] Leo Breiman. Random forests. *Machine learning*, 45(1):5–32, 2001.

[4] Eric Brochu, Vlad M Cora, and Nando De Freitas. A tutorial on bayesian optimization of expensive cost functions, with application to active user modeling and hierarchical reinforcement learning. *arXiv preprint arXiv:1012.2599*, 2010.

[5] Somboon Chaemchuen, Xuan Xiao, Nikom Klomkliang, Mekhman S Yusubov, and Francis Verpoort. Tunable metal–organic frameworks for heat transformation applications. *Nanomaterials*, 8(9):661, 2018.

[6] Eliodoro Chiavazzo, Charles W Gear, Carmeline J Dsilva, Neta Rabin, and Ioannis G Kevrekidis. Reduced models in chemical kinetics via nonlinear data-mining. *Processes*, 2(1):112–140, 2014.

[7] Bradley Efron. *Model Selection Estimation and Bootstrap Smoothing*. Division of Biostatistics, Stanford University, 2012.

[8] Jerome H Friedman. Multivariate adaptive regression splines. *The annals of statistics*, pages 1–67, 1991.

[9] Hiroyasu Furukawa, Felipe Gandara, Yue-Biao Zhang, Juncong Jiang, Wendy L Queen, Matthew R Hudson, and Omar M Yaghi. Water adsorption in porous metal–organic frameworks and related materials. *Journal of the American Chemical Society*, 136(11):4369–4381, 2014.

[10] M Hutchinson. Citrine informatics lolo, 2016.

[11] Felix Jeremias, Dominik Fröhlich, Christoph Janiak, and Stefan K Henninger. Advancement of sorption-based heat transformation by a metal coating of highly-stable, hydrophilic aluminium fumarate mof. *RSC advances*, 4(46):24073–24082, 2014.

[12] Felix Jeremias, Vasile Lozan, Stefan K Henninger, and Christoph Janiak. Programming mofs for water sorption: amino-functionalized mil-125 and uio-66 for heat transformation and heat storage applications. *Dalton transactions*, 42(45):15967–15973, 2013.

[13] Anupam Khutia, Holger Urs Rammelberg, Thomas Schmidt, Stefan Henninger, and Christoph Janiak. Water sorption cycle measurements on functionalized mil-101cr for heat transformation application. *Chemistry of Materials*, 25(5):790–798, 2013.

[14] Diederik P Kingma and Jimmy Ba. Adam: A method for stochastic optimization. *arXiv preprint arXiv:1412.6980*, 2014.

[15] Harold J Kushner. A new method of locating the maximum point of an arbitrary multipeak curve in the presence of noise. *Journal of Basic Engineering*, 56(97-106), 1964.

[16] Julia Ling, Maxwell Hutchinson, Erin Antono, Sean Paradiso, and Bryce Meredig. High-dimensional materials and process optimization using data-driven experimental design with well-calibrated uncertainty estimates. *Integrating Materials and Manufacturing Innovation*, 6(3):207–217, 2017.

[17] Søren N Lophaven, Hans Bruun Nielsen, Jacob Sondergaard, and A Dace. A matlab kriging toolbox. *Technical University of Denmark, Kongens Lyngby, Technical Report No. IMMTR-2002*, 12, 2002.

[18] Jonas Mockus, Vytautas Tiesis, and Antanas Zilinskas. The application of bayesian methods for seeking the extremum. *Towards global optimization*, 2(117-129):2, 1978.

[19] Carl Edward Rasmussen and C Williams. Gaussian processes for machine learning the mit press. *Cambridge, MA*, 2006.

[20] Tsuyoshi Ueno, Trevor David Rhone, Zhufeng Hou, Teruyasu Mizoguchi, and Koji Tsuda. Combo: an efficient bayesian optimization library for materials science. *Materials discovery*, 4:18–21, 2016.

[21] Stefan Wager, Trevor Hastie, and Bradley Efron. Confidence intervals for random forests: The jackknife and the infinitesimal jackknife. *The Journal of Machine Learning Research*, 15(1):1625–1651, 2014.